Revision 1

Hydrothermal chloritization process from biotite in the Toki granite, Central Japan: Temporal variation of chemical characteristics in hydrothermal fluid associated with the chloritization

Takashi Yuguchi [1]*, Eiji Sasao [1], Masayuki Ishibashi [1], and Tadao Nishiyama [2]

[1] Mizunami Underground Research Laboratory, Geoscientific Research Department, Sector of Decommissioning and Radioactive Waste Management, Japan Atomic Energy Agency, 1-64, Yamanouchi, Akiyo, Mizunami, Gifu 509-6132, Japan.

[2] Department of Earth and Environmental Sciences, School of Science, Graduate School of Science and Technology, Kumamoto University, 2-39-1, Kurokami, Chuo-ku, Kumamoto 860-8555, Japan.

* Corresponding author: T. Yuguchi

E-mail address: yuguchi.takashi@jaea.go.jp

Tel: +81 572 66 2244 / Fax: +81 572 66 2245

ABSTRACT

This paper describes the biotite chloritization process with a focus on mass transfer in the Toki granitic pluton, Central Japan, and also depicts the temporal variations in chemical characteristics of hydrothermal fluid associated with chloritization during the sub-solidus cooling of the pluton. Singular value decomposition (SVD) analysis results in chloritization reaction equations for eight mineral assemblages, leading to the quantitative assessment of mass transfer between the reactant and product minerals, and inflow and outflow of components through the hydrothermal fluid. The matrices for SVD analysis consist of arbitrary combinations of molar volume and closure component in the reactant and product minerals. The eight reactions represent the temporal variations of chemical characteristics of the hydrothermal fluid associated with chloritization: the progress of chloritization results in gradual increase of silicon, potassium and chlorine and gradual decrease of calcium and sodium in the hydrothermal fluid with temperature decrease. The biotite chloritization involves two essential formation mechanisms: 'CF (chlorite formation) mechanism 1', small volume decrease from biotite to chlorite and large inflow of metallic ions such as Al^{3+}, Fe^{2+}, Mn^{2+} and Mg^{2+} from the hydrothermal fluid, and 'CF mechanism 2', large volume decrease and large outflow of the metallic ions into hydrothermal fluid. Chlorite produced with 'CF mechanism 1' dominates over that of 'CF mechanism 2', resulting in the gradual decrease of the metallic components in the hydrothermal fluid with chloritization progress. The chloritization reactions also give the temporal variations in physicochemical parameter of the hydrothermal fluid: a gradual decrease of pH and a gradual increase of redox potential in the hydrothermal fluid as chloritization proceeds.

The combination of continuous reactions based on compositional variations in chlorite together with corresponding continuous Al^{IV} variations gives an indication of the temporal variations in rates of decreasing and increasing concentration of chemical components in the hydrothermal fluid associated with chloritization. The biotite chloritization and resultant temporal variations of chemical and physicochemical characteristics in hydrothermal fluid act as a "trigger" for the successive dissolution – precipitation process of a granitic rock.

Keywords: Chloritization; Fluorine-bearing Biotite; Hydrothermal Fluid; Tetrahedral Aluminium in Chlorite; Singular Value Decomposition (SVD) Analysis.

INTRODUCTION

This study focuses on biotite chloritization in granite due to hydrothermal alteration. Hydrothermal alteration influences the geochemical features in a granitic rock (Ferry, 1979). The degree and extent of the hydrothermal alteration in a granitic rock has a significant effect on weathering processes, which also influence the chemical characteristics of the groundwater due to water-rock interaction. Nishimoto and Yoshida (2010) described how the hydrothermal alteration in the granitic rock is constrained mainly by the dissolution – precipitation process during the infiltration of hydrothermal fluid along microcracks. The hydrothermal alteration of the granite progressed through three successive stages: 1) partial dissolution of plagioclase and partial chloritization of biotite, 2) biotite chloritization and precipitation of corrensite and smectite in the dissolution pores of plagioclase, and 3) dissolution of K-feldspar, the chlorite, corrensite and smectite and precipitation of illite (i.e. sericitization). In such a hydrothermal alteration process, biotite chloritization occurs under a wide temperature range below about 400 ^{o}C (e.g. De Caritat et al., 1993; Yoneda and Maeda, 2008) and occurs ubiquitously throughout the granitic rock body. Chlorites of hydrothermal origin in granitic rocks record the chemical characteristics of the hydrothermal fluid, which will therefore provide an important clue to the nature of alteration reactions and mass transfer due to hydrothermal fluid advection in the granitic pluton through a wide temperature range during sub-solidus cooling.

The biotite chloritization reaction in granitic rocks has been described in previous studies (e.g. Gresens, 1967; Gilkes and Suddhiprakarn, 1979; Parry and Downey, 1982; Parneix et al., 1985; Eggleton and Banfield, 1985; Pozzuoli et al., 1992; Wilamowski,

2002). Representative hydrothermal chloritization was demonstrated by hydrolysis reactions such as an Al conservation reaction by Ferry (1979) and a Ti conservation reaction by Parneix et al. (1985). These reactions are accompanied by breakdown products such as titanite, Ti-oxide, epidote and dolomite, indicating addition (inflow) of Fe and Mg to biotite and release of K from biotite. No deformation signature both in the biotite and in the chloritization products implies there is a constant solid volume between them (see below, petrography). However, these authors did not take account of the volume relation between reactants and products to derive the reactions. Parry and Downey (1982) presented a volume conserved reaction with chlorite as the only breakdown product. Thus, previous studies have not given a reasonable reaction for the natural observation of biotite chloritization in granitic rocks, which should be a volume-conserved reaction with several associated minerals.

This paper presents the petrography and chemistry of the chloritization in the Toki granitic pluton involving mineral assemblages, textures, and compositions. The Toki granite in the Tono district, Central Japan, is one of the Late Cretaceous plutonic intrusives in the Sanyo Belt, the Inner Zone of Southwest Japan (Fig. 1; Ishihara and Chappell, 2007). A series of studies by the authors have presented the processes from intrusion through emplacement to cooling of the Toki granitic pluton (Yuguchi et al., 2010, 2011b, 2011c, 2011d, 2013). The Toki granite is a good candidate for such studies because several occurrences (types) of chloritization are recognized in terms of mineral assemblage (see petrography below). Thus, investigation of mass transfer and temperature conditions in each occurrence will identify temporal changes in the chloritization mechanism (i.e. chloritization process) during sub-solidus cooling, reflecting temporal variations of chemical characteristics in hydrothermal fluids

104 responsible for the chloritization.

105

THE TOKI GRANITE

The Naegi – Agematsu granite and the Nohi rhyolite, distributed in Central Japan, were formed as a volcanic – plutonic complex in a shallow crust along an active continental margin, attributed to the subduction of the Kula – Pacific ridge beneath the Eurasian continent (Nakajima, 1994; Sonehara and Harayama, 2007). The Toki granitic body is a member of the Naegi – Agematsu granite. The Toki granite is a stock, about 14 × 12 km^2 in areal extent (Ishihara and Suzuki, 1969), intrusive into Jurassic sedimentary rocks of the Kamiaso unit in the Mino Terrane (Sano et al., 1992) as well as into the late Cretaceous Nohi rhyolite, of which the chemical Th-U-total Pb isochron (CHIME) age of allanite is 85 ± 5 Ma (Suzuki et al., 1998) (Fig. 2A). The Toki granite has a whole-rock Rb-Sr age of 72.3 ± 3.9 Ma (Shibata and Ishihara, 1979), and a monazite CHIME age of 68.3 ± 1.8 Ma (Suzuki and Adachi, 1998). The Toki granite also has biotite K-Ar ages of 78.5±3.9 to 59.7±1.5 Ma and zircon fission-track ages of 75.6± 3.3 to 52.8±2.6 Ma (Yuguchi et al., 2011d). On the basis of phase relationships, Yamasaki and Umeda (2012) estimated that the emplacement depth of the granitic magma was about 5–7 km below surface. The Toki granite is overlain unconformably by the Miocene Mizunami Group and the Mio-Pleistocene Tokai Group (Itoigawa, 1974; 1980; Todo Collaborative Research Group, 1999).

The Toki granite, a zoned pluton, has three rock facies grading from muscovite-biotite granite (MBG) at the margin through hornblende-biotite granite (HBG) to biotite granite (BG) in the interior (Fig. 2B). The boundaries of the three rock facies are defined by the appearance (MBG / HBG) and disappearance (HBG / BG)

of hornblende without a chilled margin. The systematic change in the Alumina Saturation Index (ASI) values from MBG through HBG to BG, corresponds to a systematic variation in the bulk chemistry, from peraluminous at the margin to metaluminous in the interior (Yuguchi et al., 2010).

The characteristics of hydrothermal alteration in the Toki granite were described comprehensively in Nishimoto et al. (2008) and Nishimoto and Yoshida (2010). Illitization (sericitization) of plagioclase and chloritization of biotite are ubiquitous throughout the rock body (both in the intact part and fractured part). Nishimoto and Yoshida (2010) concluded that the hydrothermal alteration in the Toki granite proceeded through three successive stages (as described in the Introduction).

SAMPLING AND ANALYTICAL PROCEDURES

The Mizunami Underground Research Laboratory is located on the sedimentary Mizunami Group unconformably overlying the Toki granite (Fig. 2A and 3A). The underground facilities of the Mizunami Underground Research Laboratory consist of two vertical shafts (Main and Ventilation Shafts), horizontal tunnels connecting the two shafts every 100 m depth, Measurement Niches (at 200 m and 300 m depth from ground level) and an Access/Research Gallery (300 m depth) (Fig. 3B). The unconformity between the Mizunami Group and the Toki granite is intersected by the shafts at about 170 m depth. At present, in 2014, both the Main and Ventilation Shafts are 500 m deep, ranging from an altitude of 201 masl (meters above sea level) (ground level) to an altitude of -299 masl (shaft bottom). Borehole 06MI03 (336 m long) used in this study, is vertical, drilled from an underground depth of 191 m, before continuing the excavation of the Ventilation Shaft below 191 m depth (Fig. 3B). The rock mass around 500 m depth (altitude: -299 masl) in the Ventilation Shaft (Fig. 3B), the bottom of HBG in rock facies, has the highest biotite mode (up to 10.3 vol %) and the highest chlorite mode (up to 3.2 vol %) in the Toki granite. Thus, the samples were collected from the deepest part of borehole 06MI03, in the range from an altitude of -274 masl to -314 masl (9 samples spaced 5 meters apart). Such sampling from a restricted portion has the merit of providing rock samples that have undergone the same temperature and pressure history in the sub-solidus cooling process of the Toki granite.

Minerals were analyzed with an energy-dispersive X-ray microanalyzer (JEOL JSM-7001F field emission SEM equipped with an Oxford INCA X-Max EDS system) housed at Kumamoto University, operating at an accelerating voltage of 15 kV, and a

beam current of 1.0 nA and with a beam area of 2×2 μm^2. Fluorite (CaF_2) and halite (NaCl) crystals were adopted as standard material for quantitative analysis of fluorine and chlorine concentration. The EDS is equipped with a large-caliber X-ray detector (20 mm^2) and a spectral separation program, having high resolution for low energy elemental lines, typically fluorine and chlorine Kα line.

PETROGRAPHY

Sample descriptions

The mineral assemblage consists of quartz + plagioclase + K-feldspar + biotite ± hornblende ± muscovite, with accessory minerals such as zircon, apatite, ilmenite, magnetite, and secondary minerals such as chlorite, titanite, epidote, allanite, sericite and calcite. Quartz occurs as equigranular crystals 0.5-25 mm across, ranging from 20.1 to 32.6 vol % of each thin section. Plagioclase (24.8 to 33.8 vol %) occurs as subhedral to euhedral crystals, 1 – 20 mm across with normal zoning. Secondary sericite typically occurs in the plagioclase cores. K-feldspar (26.8 to 41.0 vol %) is present as subhedral crystals, 1-12 mm across with perthitic texture. Biotite is variably altered, partially or wholly replaced by chlorite. The modes of biotite and chlorite in each thin section range from 4.6 to 10.3 vol % and from 0.7 to 3.2 vol %, respectively. Calcite and epidote occur only as fracture-filling minerals in the Toki granite.

Unaltered Biotite

Unaltered biotite occurs as anhedral crystals more than 500 μm across, usually forming aggregates of several grains (Fig. 4). The unaltered biotite has apatite, zircon magnetite and ilmenite inclusions (Fig. 4; Table 1). The composition of unaltered biotite varies over a small range from annite to siderophyllite in the classification diagram (Fig. 5A). The unaltered biotite includes a fluorine content ranging from 0.34 to 0.79 wt% (mean value: 0.55 wt%, N=17; Table 1).

Biotite chloritization

Chlorite occurs as two types: [Type A] chlorite partially replacing biotite and [Type B] chlorite totally replacing biotite. Type A accounts for over 60 % of the total amount of chloritization.

Type A: Chlorite partially replacing biotite. Type A denotes chlorite partially replacing biotite as shown in Fig.6, in which the distribution of biotite and chlorite in the chloritization grain is shown by elemental K mapping. Biotite exhibits composition from annite to siderophyllite in a range slightly wider than that of the unaltered biotite (Fig. 5A). The biotite has fluorine content ranging from 0.20 to 0.79 wt% (mean value: 0.50 wt%, N=68; Table 1), and the minimum value is lower than that of the unaltered biotite. Chloritization proceeds from rim to core in biotite along its cleavage (Fig. 6). Chlorite composition ranges from 5.33 to 6.20 atoms per formula unit (apfu) in Si (mean: 5.78 apfu, N=102) with an almost constant Fe / (Fe + Mg) of 0.7, corresponding to ripidolite, brunsvigite and daphnite in the classification diagram of Hey (1954) (Fig. 5B). Fluorine content in chlorite is lower than that of biotite. However, chlorite does contain fluorine up to 0.44 wt%, and thus biotite and chlorite are not identified by elemental F mapping (Fig. 6). No deformation texture is observed inside the chloritized grain (Fig. 6). Chlorite is associated with minerals such as titanite, ilmenite, K-feldspar and fluorite. Type A is further subdivided into the following five sub-types (Types A-1 to A-5) by the assemblage of product minerals due to chloritization (Table 2; Fig. 6).

Type A-1: chlorite, titanite and ilmenite products

Type A-2: chlorite and fluorite products

Type A-3: chlorite and ilmenite products

Type A-4: chlorite, titanite, ilmenite and fluorite products

Type A-5: chlorite, titanite and K-feldspar products

Titanite occurs inside chlorite and at the boundary between biotite and chlorite, which is aligned parallel to cleavage of biotite with lamella shapes (several μm width) and patchy shapes (more than 10 μm width) (Fig. 6). Titanite of Type A includes a fluorine content ranging from 0.71 to 1.54 wt% (mean value: 1.02 wt%, N=10; Table 1). Lamella-shaped ilmenite (several μm width) and patchy-shaped ilmenite (more than 10 μm in minor axis) occur in chlorite, and their elongations are oriented parallel to cleavage of biotite (Fig. 6). Anhedral fluorite up to about 200 μm across occurs only in chlorite (Type A-2 of Fig. 6). The Type A-5 chloritization involves an appearance of K-feldspar. Biotite fragments up to 50 μm across are distributed in the central part of the grain. K-feldspar is distributed around biotite and chlorite with an almost homogeneous composition of Or99Ab1 (Tables 3). Euhedral magnetite and euhedral apatite are observed inside both biotite and chlorite (e.g. Type A-1 of Fig. 6), which are irrelevant to the chloritization reaction.

Type B: Chlorite totally replacing biotite. Type B represents chlorite completely replacing biotite (chlorite pseudomorph after biotite) in the hydrothermal alteration (Fig. 7). There is no systematic difference in grain size between Type A and B. Chlorite in the Type B contains Si ranging from 5.34 to 5.59 apfu (mean: 5.45 apfu, N=38), which is smaller in range relative to that of the Type A and the minimum value is almost the same (Fig. 5B). The chlorite corresponds to ripidolite in the classification

241 diagram with a constant Fe / (Fe + Mg) of 0.7. Fluorine content of chlorite in Type B
242 ranges from 0.00 to 0.22 wt% (mean value: 0.02 wt%, N=38; Table 1). No
243 deformation texture is observed inside the grains of the Type B (Fig. 7). Type B
244 chloritization is accompanied by various minerals such as titanite, ilmenite, K-feldspar
245 and fluorite. Type B is also divisible into the following three sub-types (Types B-1 to
246 B-3) according to the mineral assemblage of chloritization products (Table 2 and Fig.
247 7).
248 Type B-1: chlorite, titanite and fluorite products
249 Type B-2: chlorite and titanite products
250 Type B-3: zoned texture of product minerals including ilmenite, titanite, chlorite,
251 fluorite and K-feldspar
252 Titanite in the Type B-1 and B-2 occurs frequently with a patchy shape (more than
253 10 μm width) and infrequently with a lamella shape (several μm width), which includes
254 fluorine content ranging from 0.71 to 1.54 wt% (mean value: 1.42 wt%, N=17; Table 1).
255 Type B-3 is characteristically zoned, with associated minerals including ilmenite,
256 titanite, chlorite, fluorite and K-feldspar (from core to rim) in the core of plagioclase
257 (Fig. 7), which is infrequently observed.
258

DISCUSSION

Chloritization reactions

The chloritization reactions, satisfying both the assemblage of product minerals and the volume relationship between reactant and products, were studied based on singular value decomposition (SVD) analysis (e.g. Fisher, 1989; 1993). The reaction equation gives the quantitative mass transfer between reactant and product minerals and for the inflow and outflow of components with chloritization. The SVD analysis provides a simple and powerful method for determining univariant reactions in multicomponent mineral assemblage without considering T, P, fO_2 and pH constraints (Fisher, 1989; 1993). Several SVD analyses have been applied to model possible reaction relationships between mineral assemblages in natural metamorphic examples (e.g. Lang, 1991; Whitney et al., 1995; Lang et al., 2004; Yuguchi et al., 2011a). The SVD analysis is closely related to least squares methods, which enables to determine precise mass balance relationships in multicomponent mineral assemblage on the basis of mineral analyses involving possible analytical errors (Fisher, 1989). It can also be used for analysis of open-system reactions (Shigeno et al., 2012). Thus, the SVD analysis can be applied to studied chloritization. To determine chloritization reactions in an open system, we have to specify some conservation conditions in the SVD analysis. Previous studies defined closure components as conservation conditions in the SVD analysis. No deformation texture is observed within the chloritized grains of types A and B (Figs. 6 and 7), indicating constant solid volume replacement from reactant biotite to chloritization products. We newly defined the volume constraint as a conservation condition in the analysis. We assume one or

283 more additional condition(s) of closure components among nine components (Si, Ti, Al,
284 Fe, Mn, Mg, Ca, Na and K) for deriving the reaction relation. Thus, the matrices for
285 SVD analysis consist of arbitrary combinations of molar volume and closure
286 component(s) in the reactant and product minerals (phases) (Table 4). The
287 composition matrix of the closure components is expressed in terms of atoms of element
288 per formula unit for the mineral. Molar volume matrix is calculated on the basis of
289 composition of each mineral (see captions of Tables 1 and 3). The free software
290 program Scilab (Scilab Enterprises S.A.S) was used to conduct the SVD analysis.
291 The most reasonable reaction among the possible reaction relationships is identified
292 according to 1) the signs of stoichiometric coefficients of reactants (minus) and products
293 (plus) and 2) the least difference from the volume fraction of product minerals in the
294 observation (Table 2). Table 5 shows the most reasonable reaction equations leading
295 to chloritization in each type, which is derived from the matrices of Table 4.
296
297 **Type A-1: Chlorite partially replacing biotite (Bt → Chl + Ttn + Il).** In the
298 chloritization of Type A-1, biotite (chemical composition of the analysis No. 140 in
299 Table 1; analysis number corresponds to location shown in Fig. 6) is the reactant and
300 chlorite (No. 154), titanite (No. 131) and ilmenite (No. 158) are products. The
301 volume fraction of the product minerals expressed as a ratio; chlorite to titanite to
302 ilmenite = 1: 0.100 : 0.074 (Table 2). We consider a hydrolysis reaction in an open
303 system as follows:
304 *a* Bt + X (open components including H_2O and H^+) = *b* Chl + c Ttn + *d* Il + Y (open
305 components including H_4SiO_4)
306 where X denotes influx of chemical components through an intergranular medium

(hydrothermal fluid) and Y denotes efflux from the system. The SVD analysis determines stoichiometric coefficients *a, b, c* and *d* and those of open components involved in X and Y. Some matrices consisting of arbitrary combinations of molar volume and one or more condition(s) of closure components among the nine components Si, Ti, Al, Fe, Mn, Mg, Ca, Na and K, excluding open components for the four phases (Chl, Ttn, Il and Bt) give several possible reactions. The matrices consisting of molar volume and Ti component (Table 4) gives the following two equations:

149.8 a = 212.0 b + 56.1 c + 32.0 d (constant solid volume)

0.41 a = 0.68 c + 0.98 d (closure condition for Ti)

The SVD analysis solving the two equations gives the most reasonable reaction among several possible reactions as follows:

$$0.810\mathrm{Bt} + 0.453\mathrm{Al^{3+}} + 0.718\mathrm{Fe^{2+}} + 0.100\mathrm{Mn^{2+}} + 0.248\mathrm{Mg^{2+}} + 0.078\mathrm{Ca^{2+}} + 3.933\mathrm{H_2O} + 7.560\mathrm{H^{+}} \rightarrow 0.508\mathrm{Chl} + 0.083\mathrm{Ttn} + 0.282\mathrm{Il} + 1.567\mathrm{H_4SiO_4} + 1.554\mathrm{K^{+}} + 0.243\mathrm{F^{-}} + 0.011\mathrm{Cl^{-}}$$ (Table 5)

The reaction gives the volume fraction of the product minerals; chlorite to titanite to ilmenite = 1: 0.043 : 0.084 (Table 5).

Type A-2: Chlorite partially replacing biotite (Bt → Chl + Fl). The chloritization of Type A-2 has biotite (No. 16) as the reactant and chlorite (No. 21) and fluorite (ideal CaF_2 is assumed) as products (Table 1). The same analysis as Type A-1 gives a reasonable reaction (Table 5) on the basis of matrices including molar volume and Al component for three phases (Table 4). In the case of Type A-1, titanium was taken as the closure component to establish the chloritization reaction. However, no

Ti-bearing mineral occurs in Type A-2; therefore aluminum was taken as the closure component. The reaction represents the production of chlorite and fluorite by consumption of biotite with inflow of Fe^{2+}, Mn^{2+}, Mg^{2+}, Ca^{2+}, F^-, H_2O and H^+ from the hydrothermal fluid, accompanied by outflow of H_4SiO_4, Ti^{2+}, K^+ and Cl^- into the hydrothermal fluid (Table 5).

Type A-3: Chlorite partially replacing biotite (Bt → Chl + Il). In Type A-3, biotite (No. 192) is a reactant and chlorite (No. 191) and ilmenite (No. 215) are products (Table 3). The most reasonable reaction (Table 5) is calculated on the basis of matrices describing conservation conditions for molar volume and Ti component among three phases (Table 4). The chlorite and ilmenite are produced by consumption of biotite with inflow of Al^{3+}, Fe^{2+}, Mn^{2+}, Mg^{2+}, Ca^{2+}, H_2O and H^+ from, accompanied by outflow of H_4SiO_4, K^+, F^- and Cl^- into the hydrothermal fluid.

Type A-4: Chlorite partially replacing biotite (Bt → Chl + Ttn + Il + Fl). The chloritization of Type A-4 is characterized by biotite (No. 266) as the reactant and chlorite (No. 282), titanite (No. 318), ilmenite (No. 316) and fluorite (ideal CaF_2 is assumed) as products (Table 3). The SVD analysis of the matrices consisting of three conservation constraints of molar volume and Ti and Mn components for five phases (Table 4) gives the most reasonable reaction relation (Table 5). The chloritization products are produced by consumption of biotite with inflow of Al^{3+}, Fe^{2+}, Mg^{2+}, Ca^{2+}, H_2O and H^+ accompanied by outflow of H_4SiO_4, K^+, F^- and Cl^- into the hydrothermal fluid.

Type A-5: Chlorite partially replacing biotite (Bt → Chl + Ttn + Kfs). The reactant mineral of Type A-5 is biotite (No. 328 of Table 3) and products are chlorite (No. 339), titanite (No. 346) and K-feldspar (No. 350). The most reasonable reaction of Type A-5 chloritization (Table 5) is given by the matrices including three conservation constraints of molar volume and Ti and Mn components for four phases (Table 4). The reaction shows that the chlorite, titanite and K-feldspar formed by consumption of biotite with influx of Ca^{2+}, Na^{+}, H_2O and H^{+} accompanied by removal of H_4SiO_4, Al^{3+}, Fe^{2+}, Mg^{2+}, K^{+}, F^{-} and Cl^{-} into the hydrothermal fluid.

Type B-1: Chlorite totally replacing biotite (Bt → Chl + Ttn+ Fl). In Type B-1, the product minerals consist of chlorite (analysis No. 61 of Table 3), titanite (No. 54) and fluorite (ideal CaF_2 is assumed). Because biotite in Type B-1 was totally replaced by chlorite, the original composition of biotite is unknown. Here, we take the unaltered biotite (No. 14 of Table 1) to be a representative original mineral, because it occurs a short distance from the fully chloritized grain of Type B-1 in the same thin section. The matrices, including three conservation constraints of molar volume, and Ti and Mn components for four phases (Table 4) leads to the most reasonable reaction of the Type B-1 chloritization (Table 5). The chloritization reaction shows that the chlorite, titanite and fluorite formed by consumption of biotite with influx of Ca^{2+}, F^{-}, H_2O and H^{+} accompanied by removal of H_4SiO_4, Al^{3+}, Fe^{2+}, Mg^{2+}, K^{+}, and Cl^{-} into the hydrothermal fluid.

Type B-2: Chlorite totally replacing biotite (Bt → Chl + Ttn). Type B-2 has chlorite (No. 176 of Table 1) and titanite (No. 181) as products. The chemical

composition of the reactant biotite is given by that of a neighboring biotite in the same thin section (analysis No. 193 of Type A-3; Table 3). The SVD analysis on the basis of matrices including three conservation constraints of molar volume and Ti and Mn components for four phases (Table 4) gives the reasonable reaction of Type B-2 chloritization (Table 5). The reaction equation indicates that the chloritization is produced by consumption of biotite with inflow of Al^{3+}, Mg^{2+}, Ca^{2+}, H_2O and H^+ accompanied by outflow of H_4SiO_4, Fe^{2+}, K^+, F^- and Cl^- into the hydrothermal fluid.

Type B-3: Chlorite totally replacing biotite (Bt → Chl + Ttn + Il + Kfs + Fl). The chloritization of Type B-3 resulted in the zoned texture of chlorite (No. 227 of Table 3), titanite (No. 218), ilmenite (No. 221), K-feldspar (No. 233) and fluorite (ideal CaF_2) in the plagioclase core. The chemical composition of the reactant biotite is given by that of a neighboring biotite inclusion, which is located in the lower part of the zoned texture (see No. 257 in Fig. 7 and Table 3). The most reasonable reaction (Table 5) was derived by the matrices of two conservation constraints including molar volume and Al component for six phases (Table 4). The reaction shows that the chlorite, titanite, ilmenite, K-feldspar and fluorite formed by consumption of biotite with influx of Ti^{2+}, Mn^{2+}, Ca^{2+}, Na^+, H_2O and H^+ accompanied by outflow of H_4SiO_4, Fe^{2+}, Mg^{2+}, K^+, F^- and Cl^- into the hydrothermal fluid.

The biotite chloritization process

Integration of this study and previous studies (e.g. Veblen and Ferry, 1983; Olives and Amouric, 1984; Eggleton and Banfield, 1985; Kogure and Banfield, 2000) can present the essential chloritization process by combining crystallography and mass transfer of

chemical components. Previous studies revealed the mechanism of single chloritization from biotite (biotite-to-chlorite reaction without the associated minerals) in terms of crystallography. To compare our results with the previous studies, we divide an overall reaction into two reaction parts; one characterizes the mass transfer of chemical components in the chlorite formation (CF) reaction and the second describes the formation of the associated mineral (AMF) reaction (Table 6). Two groups have been recognized for the CF reactions: [CF mechanism 1] types A-1, A-2, A-3, A-4 and B-2 and [CF mechanism 2] types A-5, B-1 and B-3. 'CF mechanism 1' is characterized by a small volume decrease (6-20%) from biotite to chlorite with large inflow of metallic ions (Al^{3+}, Fe^{2+}, Mn^{2+} and Mg^{2+}) from the hydrothermal fluid into octahedral sheet in chlorite (Table 6). Hereafter, Al^{3+}, Fe^{2+}, Mn^{2+} and Mg^{2+} constituting octahedral components of chlorite is simply referred to as 'metallic ions (or components)'. 'CF mechanism 2' is defined by a large volume decrease (27-63%) from biotite to chlorite with no or very little inflow of 'metallic ion(s)' from the hydrothermal fluid (Table 6). Chloritization in 'CF mechanism 1' dominates over that of 'CF mechanism 2': the former accounting for over 85 % of the total amount of chloritization.

Veblen and Ferry (1983) reported that two biotite layers became a single chlorite layer, due to the inheritance of an octahedral sheet together with the loss of an adjacent tetrahedral sheet and a potassium interlayer sheet in one biotite layer (Fig. 8). This mechanism of 'two biotite layers converted into one chlorite layer (2Bt – 1Chl)' accounts for 'CF mechanism 2' in terms of the mass transfer of chemical components (Fig. 8 and Table 6). The reaction of 'CF mechanism 2' (as represented by Type A-5 of Table 6) accompanies an addition of H_2O and hydrogen to biotite with removal of

427 silicon, potassium, fluorine, chlorine and 'metallic ions'. This reaction indicates that
428 the single chloritization from biotite does not require the supply of chemical
429 components (other than H_2O and H^+) from the hydrothermal fluid, and also shows the
430 large release of tetrahedral components (especially, silicon) and interlayer potassium
431 from biotite relative to release of octahedral components (titanium, aluminum, iron and
432 magnesium). The mechanism '2Bt – 1Chl' results in vacancy and disarray of sheets
433 in the crystal structure of biotite (Fig. 8; Eggleton and Banfield, 1985), which is
434 consistent with the feature of the CF reaction in terms of the large volume decrease
435 from biotite to chlorite.

436 The reaction of 'CF mechanism 1' (as represented by Type A-1 of Table 6) shows
437 the influx of aluminum, iron, manganese, magnesium, H_2O and hydrogen ions and the
438 outflow of silicon (H_4SiO_4), titanium, potassium, fluorine and chlorine into the
439 hydrothermal fluid. As shown in the difference in outflow of silicon (H_4SiO_4)
440 between the CF reactions of 'CF mechanisms 1 and 2' (Table 6), the amount of the
441 tetrahedral ions released from biotite in 'CF mechanism 1' is smaller than that of the
442 'CF mechanism 2'. Thus, the 'CF mechanism 1' cannot be fully explained by the
443 sole mechanism '2Bt – 1Chl'. Olives and Amouric (1984) reported another
444 mechanism in which 'one biotite layer converts into one chlorite layer (1Bt – 1Chl)',
445 acting simultaneously with the mechanism '2Bt – 1Chl'. They described that a
446 potassium interlayer sheet is replaced by a 'brucite-like sheet' (Fig. 8). The CF
447 reaction of 'CF mechanism 1' shows the influx of 'metallic ions' and H_2O from the
448 hydrothermal fluid, indicates that the 'brucite-like sheet' could be produced by the
449 supplement of 'metallic ions' and H_2O. This mass transfer of chemical components
450 supports the mechanism '1Bt – 1Chl'. The 'brucite-like sheet' acts as an octahedral

sheet, resulting in one biotite layer being transformed into one chlorite layer. Kogure and Banfield (2000) explained that the replacement of a potassium interlayer sheet by a 'brucite-like sheet' is necessary for the spatial allowance in crystal geometry of biotite (e.g. vacancy and disarray of sheet). Thus, the '1Bt – 1Chl' mechanism occurs after onset of mechanism '2Bt – 1Chl'. Combination of mechanisms '1Bt – 1Chl' and '2Bt – 1Chl' are consistent with the mass transfer of chemical components in the reaction of 'CF mechanism 1', and also can explain the small volume decrease from biotite to chlorite in 'CF mechanism 1' relative to that of 'CF mechanism 2'. The factor determining which 'CF mechanisms 1' or '2' occurs is the supply of 'metallic ions' from the hydrothermal fluid. Biotite chloritization occurs at the incipient stage in the successive hydrothermal alteration of the Toki granite (Nishimoto and Yoshida, 2010). Nishimoto and Yoshida (2010) also described that the incipient stage is associated with the condition of relatively low fluid / rock ratio due to relatively low porosity and fracture density in the successive alteration stages. Low flux (fluid / rock) condition in the rock body yields the spatial heterogeneities in the chemical characteristics of the hydrothermal fluids, and which constrains the presence or absence of supplement of 'metallic ions' during chloritization (Fig. 8). Therefore, the cause determining which 'CF mechanisms 1' or '2' occurs is the low fluid (fluid / rock) condition in the granite.

The associated minerals occur in chlorite but not in biotite, which is frequently aligned parallel to cleavage of the original biotite (Figs. 6 and 7). Petrography shows the volume conservation between reactants and chloritization products, indicating that the residual vacancies due to volume decrease in the CF reaction are used for formation of the associated minerals (Fig. 8). That is, the CF reaction occurs earlier than the

AMF reaction.

Eight different assemblages of associated minerals in chloritization products are observed in the samples, which depend on neither the difference between 'Types A and B' nor on the difference between 'CF mechanisms 1 and 2' (Tables 5 and 6). Samples were collected from a restricted region in an altitude range of 40 m in the same borehole (Fig. 3), which assures that these rock samples share the same temperature and pressure history. That is, the difference of mineral assemblage is not due to temperature and pressure conditions. The composition of biotite as a reactant in chloritization shows a small variation in the samples, especially with no difference for each type (Fig. 5A). Therefore, the different mineral assemblages in the chloritization products could be constrained by the differences in the chemical components supplied from the hydrothermal fluid. Low flux (fluid / rock) condition in the rock body yields the spatial heterogeneities in the chemical characteristics of the hydrothermal fluids, which also represents the cause giving the different mineral assemblages in the chloritization products (Fig. 8). The AMF reactions with 'CF mechanisms 1 and 2' indicate that the combination of components supplied from the hydrothermal fluid and the some components decomposed from biotite produced the associated mineral (Table 6).

Temperature conditions in each chloritization type deduced from the tetrahedral aluminium occupancy

Chlorite geothermometers have been proposed on the basis of the compositional variability: 1) the empirical thermometer based on the tetrahedral aluminum occupancy as a function of temperature (e.g. Cathelineau, 1988; Kranidiotis and MacLean, 1987; Jowett, 1991) and 2) the thermodynamic thermometer based on equilibrium between

chlorite and an aqueous solution (e.g. Walshe, 1988; Vidal et al., 2001). The chemical equilibrium among reactant biotite, product chlorite and aqueous solution (hydrothermal fluid) is conditioned on utilizing a chlorite thermometer. Vidal et al. (2001) employed the tetrahedral aluminum thermometer on the assumption of chemical equilibrium between chlorite and aqueous solution under quartz saturation conditions. Some empirical studies (e.g. Cathelineau and Nieva, 1985; De Caritat et al., 1993; Yoneda and Maeda, 2008) determined that the tetrahedral aluminium in chlorite is a parameter depending on temperature conditions. The variation in not only in the tetrahedral aluminum but also that the Fe / (Fe + Mg) in chlorite should be considered in the determination of the formation temperature (Kranidiotis and MacLean, 1987; Shikazono and Kawahara, 1987; Jowett, 1991). In the Toki granite, chlorite compositions in Types A and B formation factor show that the variation of the tetrahedral aluminium (Al^{IV}) ranges from 1.80 to 2.67 apfu (mean value of 2.31 apfu, N=140) but that there is no variation in Fe / (Fe + Mg), indicating that there is no correlation between them (Fig. 5B). The above chemical observation indicates that the tetrahedral aluminium in chlorites can be used to show at least the relative difference of the chloritization temperature conditions between Types A and B.

Figure 9A shows variations of the tetrahedral aluminum (range and mean value) in chlorite with Types A and B. There is a positive correlation between Al^{IV} contents and chloritization temperature (Cathelineau, 1988). The maximum values of the tetrahedral aluminium are almost consistent between Types A and B, indicating that the chloritizations of all types started from the same temperature condition. That is, the chloritization of all types started with the same timing because the observed samples collected from the restricted region had the same temperature history. The Al^{IV}

523 contents of Type B show a small range (from 2.41 to 2.66 apfu) relative to that of Type
524 A, indicating that the chloritization of Type B continued for a short temperature interval,
525 i.e. a shorter period, relative to that of Type A. The reaction termination of Type B
526 may be caused by the entire consumption of reactant biotite in the chloritization grain.
527 Type A has chlorites with an Al^{IV} content ranging from 1.80 to 2.67 apfu (Fig. 9A).
528 The lowest value (1.80 apfu) is an indication of the lower limit of chloritization
529 temperature. The maximum- (2.67 apfu) and the minimum- (1.80 apfu) Al^{IV} among
530 chlorites of Types A and B correspond to the onset and terminal temperature of the
531 hydrothermal chloritization, respectively. The temperature intervals indicate the
532 chloritization stage in the sub-solidus cooling process of the Toki granite (Fig. 9A).
533 A rough temperature index is estimated from the chlorite thermometer of Yoneda
534 and Maeda (2008) on the assumption that the equilibrium among minerals and
535 hydrothermal fluid is established (Fig. 9B). Types A and B have the chloritization
536 temperature conditions from 350 to 180 ^{o}C and from 350 to 290 ^{o}C, respectively.
537 Types A-2 and B-2 with both of '2Bt – 1Chl' and '1Bt – 1Chl' mechanisms (CF
538 mechanism 1) show similar Al^{IV} (temperature) ranges (Fig. 9). Types A-1 and A-5
539 have different CF mechanisms: the former with both of '2Bt – 1Chl' and '1Bt – 1Chl'
540 mechanisms and the later including only '2Bt – 1Chl' mechanism (CF mechanism 2).
541 However, types A-1 and A-5 also have similar Al^{IV} (temperature) ranges (Fig. 9).
542 These observations can be interpreted by that the determination of tetrahedral aluminum
543 occupancy occurs in common '2Bt – 1Chl' mechanism among all types (Fig. 8). In
544 the '2Bt – 1Chl' mechanism, the Al^{IV} derived from the released tetrahedral sheet may
545 replace the inherited tetrahedral silicon.
546

Hydrothermal chloritization process and the associated temporal variations in chemical characteristics of the hydrothermal fluid

Temporal variations in chemical characteristics of the hydrothermal fluid deduced from the chloritization reaction. The different mineral assemblages in the chloritization products are constrained by the differences in the chemical components supplied from the hydrothermal fluid, and thus indicating the spatial heterogeneities in the chemical characteristics of the hydrothermal fluids in the restricted region. The heterogeneities (with or without 'metallic components') also determines whether 'CF mechanisms 1' or '2' occurs in chloritization. The differences between 'CF mechanisms' constrain the differences in outflow components into hydrothermal fluid. That is, the chloritization process and the chemical components in hydrothermal fluid are interdependent.

The eight overall reactions in Type A and B (Table 5) have common characteristics in terms of mass transfer: outflow of silicon, potassium and chlorine into the hydrothermal fluid. This causes the temporal variations in chemical characteristic of the hydrothermal fluid associated with the chloritization: the progress of chloritization results in gradual increase of silicon, potassium and chlorine in the hydrothermal fluid with temperature decrease. Calcium and sodium are observed only as reactants in the overall reactions (Table 5), indicating that as chloritization proceeds, there is a gradual decrease of calcium and sodium in the hydrothermal fluid with temperature decrease. Although the CF reaction is always accompanied by outflow of fluorine (Table 6), the formation of fluorite suppresses steady increase of fluorine in the hydrothermal fluid with chloritization progress.

The chloritization with 'CF mechanism 1' (Type A-1, A-2, A-3, A-4 and B-2 of

571 Table 5) gives the gradual decrease of 'metallic components' in the hydrothermal fluid,
572 while Type A-5, B-1 and B-3 with 'CF mechanism 2' results in the gradual increase of
573 'metallic components'. The petrography shows that 'CF mechanism 1' is dominant
574 over 'CF mechanism 2'. Thus, the chloritization yields gradual decrease of 'metallic
575 components' in the hydrothermal fluid with temperature decrease.

576 Chlorite derived from 'CF mechanism 2' is characterized by high Mn content, which
577 has a stoichiometric coefficient up to double that of 'CF mechanism 1' (Tables 1 and 3).
578 Thus, high Mn-bearing chlorite is formed only by the mechanism '2Bt – 1Chl' on the
579 basis of the inheritance of an octahedral sheet in a biotite, i.e. manganese content in
580 chlorite is provided from biotite and not from hydrothermal fluid (Table 6). If
581 hydrothermal fluid was rich in manganese, the chlorite composition with the 'CF
582 mechanism 1' must also be rich in manganese because the 'brucite-like sheet' is formed
583 by the supplement of 'metallic ions' from the hydrothermal fluid. This observation
584 implies that the hydrothermal fluid was not rich in manganese during the chloritization
585 stage.

586 The chloritization reactions also reveal temporal variations in potential of hydrogen
587 (pH) and redox potential of the hydrothermal fluid. Hydrogen ion is observed only as
588 a reactant in the overall reactions (Table 5). Therefore, there is a gradual decrease of
589 concentration of H^+ in the hydrothermal fluid as chloritization proceeds, indicating that
590 a gradual decrease of pH in the hydrothermal fluid. Redox potential of the
591 hydrothermal fluid is sensitive to change of ferrous ions in the fluid. The overall
592 reactions show that ferrous ions are mainly used as a reactant in the chloritization (Table
593 5). A gradual decrease of concentration of Fe^{2+} in the hydrothermal fluid occurs as
594 chloritization proceeds, which represents that a gradual increase of redox potential of

595 the hydrothermal fluid.

596 Ilmenite occurs as chloritization products in the Toki granite. Tadashi et al.
597 (1975) presents oxygen fugacity (fO_2 = about 10^{-27} atm at temperature condition of 350
598 ^{o}C) producing ilmenite with chemical composition of FeO: 32.5, MnO: 13.5 and TiO_2:
599 52.8 wt %. Such ilmenite composition is almost the same as that with chloritization
600 of the Toki granite (Table 5). Thus, the chloritization of the Toki granite may occur
601 under the fO_2 of about 10^{-27} atm. Although the temporal variation of fO_2 cannot be
602 determined, the oxygen fugacity is presumed as about 10^{-27} atm as long as ilmenite
603 formation is stable.

604

605 **Continuous temporal variations in chemical characteristics of the hydrothermal**
606 **fluid deduced from the chemical profile in a chloritization grain.** A grain in the
607 process of being chloritized, i.e. partially chloritized grain, shows the sequential
608 variation in chlorite composition, representing the progression of the chemical reactions
609 (mass transfer) and temperature conditions during chloritization. The chloritization
610 due to 'CF mechanism 1' is dominant over that of the 'CF mechanism 2'. The
611 chloritization of Type A-1 (CF mechanism 1) progresses through the chloritization
612 stages (Fig. 9A), and therefore enables us to unravel the major chloritization process
613 and the successive temporal variations in chemical characteristics of the hydrothermal
614 fluid responsible for the chloritization. The partially chloritized grain of Type A-1 of
615 Fig. 10A involves the central biotite area between two chlorite areas, named α (upper)
616 and β (lower). Figure 10B shows the compositional profiles of chlorite through
617 central biotite (α chlorite area: 160-250 μm range in the scanning line and β area: 0-90
618 μm). Although biotite has homogeneous composition except at the rims in contact

619 with chlorite, chlorite displays gradual compositional variations. In the α area, Al_2O_3,
620 FeO and MnO decrease towards biotite (from 250 to 160 μm) and SiO_2 and MgO
621 increase to biotite. In the β area, Al_2O_3, FeO and MnO show maximum
622 concentrations at about 50 μm along the scanning line, and gradually decrease from
623 there (50 μm) to both biotite sides (90 μm: rims in contact with biotite with the
624 minimum concentrations) and the rim side (0 μm). The β area also has the minimum
625 concentrations of SiO_2 and MgO at about 50 μm position in the profile, and SiO_2 and
626 MgO gradually increase from there on both sides (0 μm and 90 μm). Other
627 components do not show any obvious variations along the scanning line in the chlorite.
628 Figure 10C shows the profiles of the tetrahedral aluminum in the chlorite of Type
629 A-1. The continuous Al^{IV} variation along the scanning line indicates the change of
630 the chloritization temperature in the grain, and therefore implies the extent (e.g.
631 alteration direction) of chloritization progress with temperature decrease. In the α
632 area, the tetrahedral aluminum content corresponding to the chloritization temperature
633 decreases towards biotite (from 250 to 160 μm), indicating that the chloritization
634 progressed from the chlorite rims (250 μm) toward the interior (160 μm). The β area
635 shows the maximum Al^{IV} content at about 50 μm in the scanning line, and they decrease
636 from there to both 0 μm and 90 μm side. That is, the hydrothermal chloritization
637 started at the 50 μm position in the profile, and extended in both directions (0 μm and
638 90 μm). The onset temperature conditions in chloritization of Type A-1 are almost
639 consistent between the α and β areas: the Al^{IV} content of 2.51 apfu (about 310 ^{o}C
640 estimated by the chlorite thermometer of Yoneda and Maeda (2008); 50 μm in the β
641 area) and 2.43 apfu (about 290 ^{o}C; 250 μm in the α area). The terminal temperature

642 of chloritization is derived from the chloritization front in contact with the reactant
643 biotite, which also shows consistency between the α and β areas: the Al^{IV} content of
644 1.94 apfu (about 200 °C; 90 μm in the β area) and 1.97 apfu (about 200 °C; 160 μm in
645 the α area).

646 Combining the continuous reaction equations based on the compositional profiles in
647 the chlorite of Type A-1 (N=34; Fig. 10B) and the corresponding continuous variations
648 in the tetrahedral aluminum giving the temperature changes (Fig. 10C) leads to
649 deduction of the quantitative variation in inflow and outflow of components from and
650 into the hydrothermal fluid with the progress of chloritization. Constant
651 compositions of biotite as reactant (analysis location No. 140; Table 1), titanite (No.
652 131) and ilmenite (No. 158) as products are adopted for estimating the continuity of
653 chloritization reactions. The reaction equations were calculated on the basis of
654 matrices including molar volumes and the closure Ti component in the SVD analysis
655 (along with the above-mentioned formulization of the Type A-1). In the result, the
656 chloritization reactions (N=34) show that the chlorite, titanite and ilmenite formed by
657 consumption of biotite with influx of aluminum, iron, manganese, *magnesium,
658 calcium, H_2O and hydrogen ions accompanied by removal of silicon (silicic acid),
659 potassium, fluorine and chlorine into the hydrothermal fluid. (*Note: thirty-three
660 reaction equations show the inflow of magnesium whereas one reaction shows outflow
661 through the hydrothermal fluid.)

662 Figures 10D and E show the profiles of inflow and outflow amounts of chemical
663 components through the hydrothermal fluid with progress of Type A-1 chloritization,
664 which indicates the rates of decreasing and increasing concentrations of chemical
665 components in the hydrothermal fluid with chloritization progress. In the trend

666 towards reduction in ‘metallic components’ with chloritization progress (overall
667 reaction of the Type A-1: Table 5), the rates of decreasing concentrations of aluminum,
668 iron and manganese in the hydrothermal fluid become progressively smaller and that
669 of magnesium become progressively larger (Fig. 10D). The rate of increasing
670 concentration of silicon in the hydrothermal fluid becomes progressively smaller (Fig.
671 10E). Other components show constant rates of decreasing/increasing
672 concentrations with thermal and temporal change.
673

IMPLICATIONS

This study reveals the biotite chloritization process with a focus on mass transfer in the Toki granitic pluton, Central Japan, indicating an interdependent relationship between mineral alteration and hydrothermal fluid. Petrography shows two types chloritization; [Type A] chlorite partially replacing biotite and [Type B] chlorite totally replacing biotite. The Al^{IV} distribution in the chloritization grain implies the extent (e.g. alteration direction) of chloritization progress with temperature decrease. The chloritization is also characterized with some associated minerals such as titanite, ilmenite, K-feldspar and fluorite, and the variety of mineral assemblages enables the subdivision of types A and B into Types A-1 to A-5 and B-1 to B-3, respectively. The singular value decomposition (SVD) analysis provides an understanding of the overall reaction from biotite to chlorite with associated minerals in each type. Not only closure component but also molar volume in the reactant and product minerals are configured to establish the matrices for SVD analysis, which can serve as an effective technique for revealing the mass transfer of the hydrothermal alteration and metamorphic reaction with constant solid volume replacement. The overall reactions lead to the mass transfer between the reactant mineral and the product minerals and the associated inflow and outflow of components with respect to the hydrothermal fluid.

Combination of the mass transfer of chemical components and the previously-proposed crystallography in biotite chloritization can present the essential chloritization process. The single chloritization reactions from biotite are classified into two formation mechanisms; [CF mechanism 1] small volume decrease from biotite to chlorite and inflow of ‘metallic ions’ from the hydrothermal fluid and [CF

mechanism 2] large volume decrease and outflow of 'metallic ions'. Both mechanisms, '2Bt – 1Chl' (two biotite layers become one chlorite layer) and '1Bt – 1Chl' (one biotite layer becomes one chlorite layer), act in 'CF mechanism 1', whereas 'CF mechanism 2' involves only the '2Bt – 1Chl' mechanism. The determining factor in whether 'CF mechanisms 1' or '2' occurs is the availability and supply of 'metallic ions' from the hydrothermal fluid. Low flux (fluid / rock) condition in the rock body yields the spatial heterogeneities in the chemical characteristics of the hydrothermal fluids, and which constrains the presence or absence of supplement of 'metallic ions' during chloritization.

This paper also reveals the temporal variations in chemical characteristics of hydrothermal fluid associated with chloritization during the sub-solidus cooling of the pluton. The overall reactions represent the temporal variations in chemical characteristics of the hydrothermal fluid during the chloritization stage: the gradual increase of silicon, potassium and chlorine and gradual decrease of calcium and sodium with chloritization progress. Chlorite from 'CF mechanism 1' is dominant over that with 'CF mechanism 2'. The 'CF mechanism 1' is accompanied by large inflow of 'metallic ions' from the hydrothermal fluid. Thus, the chloritization progress provides an indication of the gradual decrease of 'metallic components' in the hydrothermal fluid with temperature decrease.

The overall reactions also reveal the temporal variations in physicochemical parameter (potential of hydrogen and redox potential) of the hydrothermal fluid: a gradual pH decrease and a gradual redox potential increase as chloritization proceeds. The altered physicochemical parameter of the fluid influenced the subsequent alteration mechanism because the hydrothermal fluid with low pH and high redox potential

722 impacts the dissolution of minerals such as plagioclase, K-feldspar, corrensite, smectite
723 and the chlorite. It is also inevitable that the chemical component released from
724 chloritization affects the mineral precipitation. Therefore, the biotite chloritization
725 and resultant temporal variations of chemical and physicochemical characteristics in
726 hydrothermal fluid act as a "trigger" for the successive hydrothermal alteration
727 (dissolution – precipitation) process of the granitic rock.
728

729 **ACKNOWLEDGEMENTS**

730

731 Technical comments and English review by Mr. G. McCrank, an ex-JAEA International
732 Fellow, are appreciated. Constructive reviews by anonymous reviewer and Dr. D.I.
733 Foustoukos (associated editor) were very helpful in revising the manuscript. The
734 authors also thank researchers of the Mizunami Underground Research Laboratory and
735 the Tono Geoscience Center, JAEA, for their discussions and suggestions.

736

737 **REFERENCES CITED**

738

739 Cathelineau, M. (1988) Cation site occupancy in chlorites and illites as a function of
740 temperature. Clay Minerals, 23, 471-485.

741 Cathelineau, M., and Nieva, D. (1985) A chlorite solid solution geothermometer. The
742 Los Azufres (Mexico) geothermal system. Contribution to Mineralogy and Petrology,
743 91, 235-244.

744 De Caritat, P., Hutcheon, I., and Walshe, J.L. (1993) Chlorite geothermometry: A review.
745 Clays and Clay Minerals, 41, 219-239.

746 Eggleton, R.A., and Banfield, J.F. (1985) The alteration of granitic biotite to chlorite.
747 American Mineralogist, 70, 902-910.

748 Ferry, J.M. (1979) Reaction mechanisms, physical conditions and mass transfer during
749 hydrothermal alteration of mica feldspar in granitic rocks from South Central Maine,
750 U.S.A. Contributions to Mineralogy and Petrology, 68, 125-139.

751 Fisher, G.W. (1989) Matrix analysis of metamorphic mineral assemblages and reactions.
752 Contributions to Mineralogy and Petrology, l02, 69-77.

753 Fisher, G.W. (1993) An improved method for algebraic analysis of metamorphic
754 mineral assemblages. American Mineralogist, 78, 1257-1261.

755 Gilkes, R.J., and Suddhiprakarn, A. (1979) Biotite alteration in deeply weathered granite.
756 I. Morphological, Mineralogical, and chemical properties. II. The oriented growth of
757 secondary minerals. Clays and Clay Minerals, 27, 349-367.

758 Gresens, R.L. (1967) Composition-volume relationships of metasomatism. Chemical
759 Geology, 2, 47-65.

760 Hey, M.H. (1954) A new review of the chlorites. Mineralogical Magazine, 30, 277-292.

761 Ishihara, S., and Chappell, B. (2007) Chemical compositions of the late Cretaceous
762 Ryoke granitoids of the Chubu District, central Japan – Revisited. Bulletin of the
763 Geological Survey of Japan, 58, 323-350.
764 Ishihara, S., and Suzuki, Y. (1969) Basement granites of the Toki uranium deposits in
765 Tono region. Reports of the Geological Survey of Japan, 232, 113-127.
766 Itoigawa, J. (1974) Geology of the Mizunami district, central Japan. Bulletin of the
767 Mizunami Fossil Museum, 1, 9-42 (in Japanese).
768 Itoigawa, J. (1980) Geology of the Mizunami district, central Japan. Monograph of the
769 Mizunami Fossil Museum, 1, 1-50 (in Japanese).
770 Japan Nuclear Cycle Development Institute (2000) Regional Hydrogeological Study
771 Project Result from 1992-1999. JNC Technical Report, JNC TN7400 2003-007,
772 Tono Geoscience Center.
773 Japan Nuclear Cycle Development Institute (2002) Master Plan of the Mizunami
774 Underground Research Laboratory Project. JNC Technical Report. JNC TN7410
775 2003-001, Tono Geoscience Center.
776 Jowett, E.C. (1991) Fitting iron and magnesium into the hydrothermal chlorite
777 geothermometer: GAC/MAC/SEG/ Joint Annual Meeting (Toronto, May 27-29,
778 1991), Program with Abstract, 16, A62.
779 Kougure, T., and Banfield J.F. (2000) New insights into the mechanism for
780 chloritization of biotite using polytype analysis. American Mineralogist, 85,
781 1202-1208.
782 Kranidiotis, P., and MacLean, W.H. (1987) Systematics of chlorite alteration at the
783 Phelps Dodge massive sulfide deposit, Matagami, Quebec. Economic Geology, 82,
784 1898-1911.

785 Lang, H.M. (1991) Quantitative interpretation of within outcrop variation in
786 metamorphic assemblage in staurolite-kyanite grade metapelites, Baltimore,
787 Maryland. Canadian Mineralogist, 29, 655-671.
788 Lang, H.M., Wacher, A.J., Peterson, V.L., and Ryan, J.Q. (2004) Coexisting
789 clinopyroxene/spinel and amphibole/spinel symplectites in metatroctolites from the
790 Buck Creek ultramafic body, North Carolina Blue Ridge. American Mineralogist, 89,
791 20-30.
792 Nakajima, T. (1994) The Ryoke plutonometamorphic belt: Cretaceous crustal section of
793 the Cretaceous Eurasian continental margin. Lithos, 33, 51-66.
794 Nishimoto, S., Ukai, E., Amano, K., and Yoshida, H. (2008) Alteration process in deep
795 granitic rock - an example of Toki granite, central Japan. Journal of the Japan Society
796 of Engineering Geology, 49, 94-104 (in Japanese with English abstract).
797 Nishimoto, S., and Yoshida, H. (2010) Hydrothermal alteration of deep fractured
798 granite: Effects of dissolution and precipitation. Lithos, 115, 153-162.
799 Olives, J. and Amouric, M. (1984) Biotite chloritization by interlayer brucitization as
800 seen by HRTEM. American Mineralogist, 69, 869-871.
801 Parneix, J.C., Beaufort, D., Dudoignon, P., and Meunier, A. (1985) Biotite chloritization
802 process in hydrothermally altered granites. Chemical Geology, 51, 89-101.
803 Parry, W.T., and Downey, L.M. (1982) Geochemistry of hydrothermal chlorite replacing
804 igneous biotite. Clays and Clay Minerals, 30, 81-90.
805 Pozzuoli, A., Vila, E., Franco, E., Ruiz-Amil, A., and Calle, C.D.L. (1992) Weathering
806 of biotite to vermicular in Quaternary lahars from Monti Ernici, Central Italy. Clay
807 Minerals, 27, 175-184.
808 Sano, H., Yamagata, T., and Horibo, K. (1992) Tectonostratigraphy of Mino terrane:

809 Jurassic accretionary complex of southwest Japan. Palaeogeography,
810 Palaeoclimatology, Palaeoecology, 96, 41-57.
811 Shibata, K., and Ishihara, S. (1979) Rb-Sr whole-rock and K-Ar mineral ages of granitic
812 rocks in Japan. Geochemical Journal, 13, 113-119.
813 Shigeno, M., Mori, Y., Shimada, K., and Nishiyama, T. (2012) Jadeites with
814 metasomatic zoning from the Nishisonogi metamorphic rocks, western Japan:
815 fluid-tectonic block interaction during exhumation. European Journal of Mineralogy,
816 24, 289-311.
817 Shikazono, N., and Kawahara, H. (1987) Compositional differences in chlorite from
818 hydrothermal altered rocks and hydrothermal ore deposits. Canadian Mineralogist,
819 25, 465-474.
820 Sonehara, T., and Harayama, S. (2007) Petrology of the Nohi Rhyolite and its related
821 granitoids: a Late Cretaceous large silicic igneous field in central Japan. Journal of
822 Volcanology and Geothermal Research, 167, 57-80.
823 Suzuki, K., and Adachi, M. (1998) Denudation history of the high T/P Ryoke
824 metamorphic belt, southwest Japan: constraints from CHIME monazite ages of
825 gneisses and granitoids. Journal of Metamorphic Geology, 16, 27-37.
826 Suzuki, K., Nakazaki, M., and Adachi, M. (1998) An 85±5 Ma CHIME age for the
827 Agigawa welded tuff sheet in the oldest volcanic sequence of the Nohi Rhyolite,
828 central Japan. Journal of earth and planetary sciences, Nagoya University, 45, 17-27.
829 Tadashi, M., Tanaka, K., and Itaya, T. (1975) Oxide and sulphide minerals in pelitic and
830 pasammitic schist from the Nagatoro district, Saitama prefecture, Japan. The Journal
831 of the Japanese Association of Mineralogists, Petrologists and Economic Geologists,
832 70, 413-424.

Todo Collaborative Research Group (1999) Fault bounded inland basin of multiple blocks: an example from the sedimentary basin of the Tokai Group around Tajimi City in Gifu Prefecture, central Japan. Earth Science, 53, 291-306.

Vidal, O., Parra, T., and Trotet, F. (2001) A thermodynamic model for Fe-Mg aluminous chlorite using data from phase equilibrium experiments and natural peltic assemblages in the 100° to 600°C, 1 to 25 kb range. American Journal of Science, 301, 557-592.

Veblen, D.R., and Ferry, J.M. (1983) A TEM study of the biotite-chlorite reaction and comparison with petrologic observations. American Mineralogist, 68, 1160-1168.

Walshe, J.L. (1988) A six-component chlorite solid solution model and the conditions of chlorite formation in hydrothermal and geothermal systems. Econic Geology, 81, 681-703.

Whitney, D.L., Lang, H.M., and Ghent, E.D. (1995) Quantitative determination of metamorphic reaction history: mass balance relations between groundmass and mineral inclusion assemblages in metamorphic rocks. Contributions to Mineralogy and Petrology, 120, 404-411.

Wilamowski, A. (2002) Chloritization and polytypism of biotite in Lomnica granite, Karkonosze Massif, Sudetes, Poland: stable isotope evidence. Chemical Geology, 182, 529-547.

Yamasaki, S., and Umeda, K. (2012) Cooling history of the Cretaceous Toki granite in the eastern Sanyo Belt, Central Japan. Japanese Magazine of Mineralogical and Petrological Sciences, 41, 39-46 (in Japanese with English abstract).

Yoneda, T., and Maeda, H. (2008) The Chemical Composition of Chlorites from Hydrothermal Ore Deposits and its Applicability to Geothermometers. Journal of

MMIJ, 124, 694-699.

Yuguchi, T., Tsuruta, T., and Nishiyama, T. (2010) Zoning of rock facies and chemical composition in the Toki granitic body, Central Japan. Japanese Magazine of Mineralogical and Petrological Sciences, 39, 50-70 (in Japanese with English abstract).

Yuguchi, T., Miyazoe T., and Nishiyama, T. (2011a) Contact metamorphism of a Cretaceous accretionary prism by the 14 Ma Okueyama granite, a single post-kinematic pluton in Central Kyushu, Japan: SVD analysis of metamorphic reactions and thermal release. American Mineralogist, 96, 308-318.

Yuguchi, T., Tsuruta, T., and Nishiyama, T. (2011b) Three-dimensional cooling pattern of a granitic pluton I: The study of exsolution sub-solidus reactions in the Toki granite, Central Japan. Journal of Mineralogical and Petrological Sciences, 106, 61-78.

Yuguchi, T., Tsuruta, T., and Nishiyama, T. (2011c) Three-dimensional cooling pattern of a granitic pluton II: The study of deuteric sub-solidus reactions in the Toki granite, Central Japan. Journal of Mineralogical and Petrological Sciences, 106, 130-141.

Yuguchi, T., Tsuruta, T., Hama, K., and Nishiyama, T. (2013) The spatial variation of initial ^{87}Sr / ^{86}Sr ratios in the Toki granite, Central Japan: Implications for the intrusion and cooling processes of a granitic pluton. Journal of Mineralogical and Petrological Sciences, 108, 1-12.

Yuguchi, T., Amano, K., Tsuruta, T., Danhara, T., and Nishiyama, T. (2011d) Thermochronology and the three-dimensional cooling pattern of a granitic pluton: An example of the Toki granite, Central Japan. Contributions to Mineralogy and Petrology, 162, 1063-1077.

881

882 **Figure captions**

883

884 **Figure 1** Map of Southwest Japan showing location of the Toki granite (Tono district -
885 TKG; square symbol) in Central Japan, together with the distribution of San-in,
886 Sanyo and Ryoke Belts in the Inner Zone of Southwest Japan, after Ishihara and
887 Chappell (2007).

888

889 **Figure 2** The Toki granitic pluton. (A) Geologic map of the Tono district showing
890 the Toki granite after Itoigawa (1980), the Mizunami Underground Research
891 Laboratory and the borehole sites. The topographic contours inside the Tono
892 district are based on Geographical Survey Institute, 1:25,000 topographic maps
893 entitled Mitake, Takenami, Toki and Mizunami. Borehole investigations at the
894 Toki granite were performed by the JAEA, for the 'Regional Hydrological Study
895 (Japan Nuclear Cycle Development Institute, 2000)' and the 'Mizunami Underground
896 Research Laboratory Project (Japan Nuclear Cycle Development Institute, 2002)'.
897 (B) Rock facies cross-section for the Toki granite along the line from X to X' on the
898 geologic map (Fig. 2A). MBG: muscovite-biotite granite, HBG: hornblende-biotite
899 granite and BG: biotite granite (Yuguchi et al., 2010).

900

901 **Figure 3** The Mizunami Underground Research Laboratory. (A) Location of shafts
902 and boreholes in the Mizunami Underground Research Laboratory. (B) Schematic
903 overview of underground facilities of the Mizunami Underground Research
904 Laboratory and the sample locations used in this study. The samples were
905 collected from the borehole 06MI03; altitude range from -274 masl (meters above sea

level) to -314 masl in the HBG of the Toki granite.

Figure 4 Backscattered electron (BSE) image and chemical maps showing elemental Si, Ti, K and F concentrations of the unaltered biotite in the Toki granite. High concentrations are indicated by warm colors and low concentrations by cold colors. Ilmenite inclusion is identified by elemental Ti concentration map. The biotite includes fluorine content without concentration gradient in the crystal from core to rim. Numbers corresponds to the analysis points listed in Table 1.

Figure 5 Chemical compositions of biotite and chlorite. (A) compositional plots of the unaltered biotite and the residual biotite with chloritization (Type A) on the classification diagram with distribution from annite to siderophyllite. Biotite compositions of the Type A show slightly wider distributions relative to that of the unaltered biotite. (B) Compositional plots of chlorite in the Type A and B on the classification diagram of Hey (1954), corresponding to ripidolite, brunsvigite and daphnite. Type A shows more silicic composition than that of Type B.

Figure 6 BSE images showing Type A chloritization (chlorite partially replacing biotite: five sub-types A-1, A-2, A-3, A-4 and A-5) and their chemical maps (elemental Si, Ti, Fe, Ca, K and F concentrations). High concentrations are indicated by warm colors and low concentrations by cold colors. Numbers correspond to the analysis points listed in Table 2. [Type A-1] The chloritization grain shows laterally-banded biotite in the central parts between α (upper) and β (lower) chlorite. Titanite is identified as high Ti and Ca concentration mineral.

930 Ilmenite has high Ti concentration without Ca concentration in the elemental maps.
931 Magnetite and apatite are identified by the highest concentrations of elemental Fe and
932 Ca maps, respectively. [Type A-2] Chlorite and fluorite highlight the central part
933 of the chloritization grain. Anhedral fluorite up to about 200 μm across occurs
934 only inside chlorite, recognized by the highest F concentration. [Type A-3] The
935 chlorite and ilmenite are distributed in the left lower part of the grain. The
936 boundary between chlorite and biotite is parallel to cleavage of biotite. [Type A-4]
937 Chloritization progresses from kink band in the central part of the grain through the
938 cleavage to interior. The γ domain shows alteration front of chloritization along the
939 cleavage. [Type A-5] Colored and colorless minerals in the chloritization grain are
940 observed in the polarizing optical microscopy (POM) image; the colored minerals
941 correspond to biotite, chlorite and titanite and the colorless mineral denotes
942 K-feldspar. K-feldspar is distributed around biotite and chlorite, recognized by
943 elemental mapping of Si. Biotite and chlorite interfaces in contact with K-feldspar
944 are markedly uneven. Notably, the chlorite intrudes into K-feldspar with fan and
945 needle shapes.
946
947 **Figure 7** BSE images of chlorite in the Type B (chlorite totally replacing biotite: three
948 sub-types of B-1, B-2 and B-3) and their chemical maps with elemental Si, Ti, Fe, Ca,
949 K and F. High concentrations are indicated by warm colors and low concentrations
950 by cold colors. Numbers corresponds to the analysis points listed in Table 4.
951 [Type B-1] Titanite shows band-like distribution in the central part of the chlorite.
952 Anhedral fluorite occurs in the bottom part of the grain (about 400 × 10 μm and 20 ×
953 10 μm). [Type B-2] Patchy titanite in the chlorite area is oriented parallel to

954 cleavage of the original biotite. [Type B-3] The zoned texture of chloritization
955 minerals including ilmenite, titanite, chlorite, fluorite and K-feldspar (from core to
956 rim) is observed in the core part of plagioclase. Ilmenite occurs in the core of the
957 zonal textures (about 50 × 20 μm). Titanite has two styles of occurrence: 1)
958 titanite surrounding ilmenite (about 70 × 40 μm) and 2) anhedral titanite located
959 between chlorite and plagioclase in the lower part of the zone (about 30 × 20 μm; Fig.
960 7). Chlorite envelops titanite (about 350 × 150 μm), and also includes fluorite
961 (about 30 × 10 μm). Anhedral K-feldspar occurs at rims of the zoning, in contact
962 with plagioclase. The crack extends from rims of plagioclase to such zones, but
963 cracking inside the zone is not observed. The plagioclase has biotite inclusions
964 (Table 4), which are located below the zone (Fig. 7). There are no cracks
965 extending from the plagioclase rim to the biotite inclusion.
966
967 **Figure 8** Schematic figure showing development of crystal geometry (after Eggleton
968 and Banfield, 1985) and mass transfer of chemical components in the chloritization
969 process. The 'CF mechanism 1' resulted from a combination of mechanisms '2Bt
970 – 1Chl' (two biotite layers become one chlorite layer) and '1Bt – 1Chl' (one biotite
971 layers becomes one chlorite layer), whereas 'CF mechanism 2' is constrained solely
972 by '2Bt – 1Chl' chloritization. The residual vacancies due to volume decrease
973 from biotite to chlorite are filled by the associated minerals.
974
975 **Figure 9** Variations (range and mean value) of the tetrahedral aluminium of chlorite in
976 the types A and B (A) and their rough chloritization temperatures deduced from the
977 Yoneda and Maeda (2008) thermometer (B).

978

979 **Figure 10** Continuous temporal variation of chemical components of the
980 hydrothermal fluid associated with the chloritization progress of the Type A-1. (A)
981 BSE image of a chloritization grain in the Type A-1 showing the central biotite area
982 between α (upper) and β (lower) chlorite areas. (B) Concentration profiles of the
983 Type A-1 from β (lower) chlorite through central biotite to α (upper) chlorite along
984 the scanning line (arrow of Fig. 10A; β chlorite area: 0-90 μm range and the α area:
985 160-250 μm). (C) The profile of tetrahedral aluminium contents in the α and β
986 chlorite area, indicating the variation of chloritization temperature. The continuous
987 chloritization reactions on the basis of compositional variation of Fig. 10B leads to
988 the profiles of inflow (D) and outflow amounts (E) of chemical components through
989 the hydrothermal fluid. These profiles (D and E) and the corresponding
990 temperature change (C) represent the rates of decreasing and increasing
991 concentrations of chemical components in the hydrothermal fluid with chloritization
992 progress. The chloritization progress changes the rates in decreasing and
993 increasing concentrations of chemical components in the hydrothermal fluid with
994 temperature decrement: the rates in decreasing concentrations of aluminum, iron and
995 manganese decrease and that of magnesium increases (D). The rate in increasing
996 concentrations of silicon in the hydrothermal fluid decreases with chloritization
997 progress (E).

998

Table 1: Representative compositions of the unaltered biotite and the chloritization minerals in the type A and type B.

Type	Unaltered biotite				Type A-1					Type A-2		Type B-2		
Sample	06MI03				06MI03					06MI03		06MI03		
No.	309mabh				309mabh					309mabh		314mabh		
Altitude	-299m				-299m					-299m		-304m		
Location	4	14	66	69	140	149	154	131	158	16	21	164	176	181
Mineral	**Bt** core	**Bt** core	**Bt** rim	**Il** inc*	**Bt** core	**Chl** core	**Chl** core	**Ttn** core	**Il** core	**Bt** core	**Chl** rim	**Chl** core	**Chl** core	**Ttn** core
(wt%)														
SiO_2	35.01	34.83	35.10	-	35.20	24.59	24.66	31.46	-	34.86	25.32	24.17	24.33	31.34
TiO_2	2.25	1.08	2.95	50.92	3.47	-	-	27.30	51.90	2.96	0.43	-	-	26.83
Al_2O_3	13.87	15.21	13.80	-	13.17	18.54	17.74	6.01	-	13.82	17.33	19.61	18.81	8.14
FeO	27.84	26.43	27.17	33.72	27.60	36.61	35.86	4.43	33.00	26.55	34.89	35.56	35.60	1.21
MnO	1.09	1.14	1.04	13.62	0.87	1.46	1.10	-	14.85	1.05	1.60	1.37	1.35	-
MgO	5.13	5.63	5.15	-	5.60	6.87	7.65	0.21	-	5.30	7.07	6.54	6.92	-
CaO	-	-	-	-	-	-	-	26.67	-	-	0.27	-	-	28.90
Na_2O	-	-	-	-	-	-	-	-	-	-	-	-	-	-
K_2O	9.50	9.71	9.48	-	9.52	-	-	0.17	-	9.58	0.43	-	-	-
F	0.64	0.79	0.51	-	0.61	0.03	-	0.97	-	0.52	-	-	-	1.66
Cl	0.22	0.05	0.10	-	0.06	0.06	0.01	0.02	-	0.03	-	0.03	-	-
Total	95.55	94.87	95.30	98.26	96.10	88.17	87.02	97.24	99.75	94.67	87.34	87.28	87.01	98.08
(atom)														
Anion	22	22	22	3	22	28	28	5	3	22	28	28	28	5
Si	5.57	5.54	5.59	-	5.56	5.54	5.61	1.04	-	5.58	5.57	5.47	5.53	1.01
Ti	0.27	0.13	0.35	0.99	0.41	-	-	0.68	0.98	0.36	0.07	-	-	0.65
Al	2.60	2.85	2.59	-	2.45	4.92	4.76	0.23	-	2.61	4.64	5.23	5.04	0.31
Fe	3.71	3.51	3.62	0.73	3.65	6.90	6.83	0.12	0.69	3.56	6.63	6.73	6.77	0.03
Mn	0.15	0.15	0.14	0.30	0.12	0.28	0.21	-	0.32	0.14	0.31	0.26	0.26	-
Mg	1.22	1.33	1.22	-	1.32	2.31	2.59	0.02	-	1.27	2.39	2.21	2.35	-
Ca	-	-	-	-	-	-	-	0.95	-	-	0.07	-	-	1.00
Na	-	-	-	-	-	-	-	-	-	-	-	-	-	-
K	1.93	1.97	1.93	-	1.92	-	-	0.01	-	1.96	0.13	-	-	-
F	0.32	0.40	0.26	-	0.31	0.03	-	0.10	-	0.26	-	-	-	0.17
Cl	0.06	0.01	0.03	-	0.02	0.06	0.01	0.00	-	0.01	-	0.01	-	-
Total	15.45	15.48	15.44	2.02	15.43	19.95	20.00	3.05	1.99	15.48	19.81	19.90	19.95	3.00
V*	149.9	149.8	149.9	-	149.8	212.1	212.0	56.1	32.0	149.8	212.1	212.1	212.1	55.4

*inclusion

**Molar volume (cm^3/mol) for biotite and chlorite were calculated according to following equation of Parry and Downey (1982):

V(biotite) = 150.6 - 3.214 [Mg / (Mg + total Fe + Ti + Mn]

V(chlorite) = 213.3 - 4.909 [Mg / (Mg + total Fe + Ti + Mn]

Molar volume for titanite and ilmenite were estimated as follows:

$V = (S_1m_1 + S_2m_2 + ... + S_nm_n) / D$ (Deer et al., 1974)

where atomic number (S) and atomic mass (m) of element 'n' and D = mineral density. Mineral densities of titanite and ilmenite are 3.48 and 4.72 g/cm^3, respectively, based on website of the 'Mineralogy Database (http://webmineral.com/)'.

Table 2: Mineral assemblage and the volume (areal) ratio of product minerals in the types A and B.

Type	Mineral assemblage		Volume (areal) ratio of product minerals*
	Reactant	Product	
Type A-1	Bt	Chl, Ttn, Il	Chl : Ttn : Il = 1 : 0.100 : 0.074
Type A-2	Bt	Chl, Fl	Chl : Fl = 1 : 0.248
Type A-3	Bt	Chl, Il	Chl : Il = 1 : 0.064
Type A-4	Bt	Chl, Ttn, Il, Fl	Chl : Ttn : Il : Fl = 1 : 0.072 : 0.003 : 0.003
Type A-5	Bt	Chl, Ttn, Kfs	Chl : Ttn : Kfs = 1 : 0.085 : 1.583
Type B-1	(Bt)	Chl, Ttn, Fl	Chl : Ttn : Fl = 1 : 0.204 : 0.161
Type B-2	(Bt)	Chl, Ttn	Chl : Ttn = 1 : 0.214
Type B-3	(Bt)	Chl, Ttn, Il, Kfs, Fl	Chl : Ttn : Il : Kfs : Fl = 1 : 0.325 : 0.048 : 0.301 : 0.012

*The volume fraction of product minerals in the chloritization grain was estimated from the areal fraction of them by simply assuming the equivalence of areal and volume fractions. The area of product minerals in the chloritization grain are identified by elemental concentration maps, and the areal ratio was calculated by image processing software (Scion image).

Table 3: Atomic ratio of the chloritization minerals in type A and B for the SVD analysis.

Type	Type A-3				Type A-4				Type A-5				Type B-1		Type B-3					
Sample No.	06MI03 314mabh				06MI03 289mabh				06MI03 289mabh				06MI03 309mabh		06MI03 319mabh					
Altitude	-304m				-279m				-279m				-299m		-309m					
Location	192	193	191	215	266	282	318	316	328	339	346	350	61	54	257	227	218	221	233	251
Mineral	**Bt** rim	**Bt** rim	**Chl** core	**Il** core	**Bt** rim	**Chl** rim	**Ttn** core	**Il** core	**Bt** core	**Chl** rim	**Ttn** rim	**Kfs** rim	**Chl** core	**Ttn** core	**Bt** core	**Chl** core	**Ttn** core	**Il** core	**Kfs** rim	**Pl** core
Anion	22	22	28	3	22	28	5	3	22	28	5	8	28	5	22	28	5	3	8	8
Si	5.54	5.56	6.05	-	5.56	5.93	1.03	0.02	5.67	5.54	1.02	3.02	5.40	1.00	5.59	5.42	1.00	-	2.99	2.63
Ti	0.41	0.42	0.13	0.99	0.35	-	0.71	0.96	0.16	-	0.80	-	-	0.68	0.31	-	0.81	0.96	-	-
Al	2.42	2.44	4.46	-	2.54	4.58	0.24	-	2.95	5.13	0.14	0.98	5.27	0.25	2.65	5.48	0.14	-	1.00	1.36
Fe	3.89	3.87	6.57	0.78	3.81	6.78	0.05	0.50	3.27	7.01	0.08	-	7.09	0.05	3.60	6.64	0.05	0.97	0.01	-
Mn	0.17	0.14	0.20	0.22	0.17	0.20	-	0.51	0.13	0.39	-	-	0.42	-	0.15	0.34	-	0.08	-	-
Mg	1.27	1.20	2.04	-	1.15	2.37	-	-	1.27	1.96	-	-	1.85	0.02	1.27	2.11	-	-	-	-
Ca	-	-	0.06	-	-	0.05	0.97	0.02	-	-	0.98	-	-	0.95	-	-	1.01	-	-	0.40
Na	-	-	-	-	-	-	-	-	-	-	-	0.01	-	-	-	-	-	-	0.02	0.60
K	1.93	1.92	0.25	-	1.89	-	-	-	1.93	-	-	0.97	-	-	1.91	-	-	-	0.98	-
F	0.16	0.20	-	-	0.27	-	0.13	-	0.27	-	0.07	-	-	0.17	0.18	-	0.09	-	-	-
Cl	0.03	0.02	0.00	-	0.03	-	0.00	-	0.01	-	-	-	-	-	0.06	0.01	-	-	-	-
Total	15.63	15.55	19.76	1.99	15.47	19.91	3.00	2.01	15.38	20.03	3.02	4.98	20.02	2.95	15.48	19.99	3.01	2.01	5.00	4.99
V*	149.9	149.9	212.2	32.0	149.9	212.1	55.6	32.1	149.8	212.3	56.2	108.8	212.3	55.1	149.8	212.2	56.2	32.3	108.7	100.5

*Molar volume (cm^3/mol) for biotite, chlorite, titanite and ilmenite were calculated according to the same method as Table 1. Molar volume for plagioclase and K-feldspar were calculated on the basis of molar volumes of their end-menbers shown in Helgeson et al. (1978).

Table 4: Matrices for SVD analysis leading to the most reasonable reaction relations in the types A and B.

Type A-1. Matrix consisting of molar volume and closure component (Ti)

	Chl	Ttn	Il	Bt
V*	211.980	56.129	32.023	149.829
Ti	0	0.68	0.98	0.41

Type A-2. Matrix consisting of molar volume and closure component (Al)

	Chl	Fl	Bt
V*	212.235	24.542	149.834
Al	4.64	0.00	2.61

Type A-3. Matrix consisting of molar volume and closure component (Ti)

	Chl	Il	Bt
V*	212.180	32.027	149.889
Ti	0.13	0.99	0.41

Type A-4. Matrix consisting of molar volume and closure components (Ti + Mn)

	Chl	Ttn	Il	Fl	Bt
V*	212.056	55.558	32.068	24.542	149.926
Ti	0.00	0.71	0.96	0.00	0.35
Mn	0.20	0.00	0.51	0.00	0.17

Type A-5. Matrix consisting of molar volume and closure components (Ti + Mn)

	Chl	Ttn	Kfs	Bt
V*	212.272	56.211	108.782	149.755
Ti	0.00	0.80	0.00	0.16
Mn	0.39	0.00	0.00	0.13

Type B-1. Matrix consisting of molar volume and closure components (Ti + Mn)

	Chl	Ttn	Bt	Bt
V*	212.330	55.107	24.542	149.765
Ti	0.00	0.68	0.00	0.13
Mn	0.42	0.00	0.00	0.15

Type B-2. Matrix consisting of molar volume and closure component (Ti + Mn)

	Chl	Ttn	Bt
V*	212.070	55.354	149.915
Ti	0	0.65	0.42
Mn	0.26	0	0.14

Type B-3. Matrix consisting of molar volume and closure component (Al)

	Chl	Ttn	Il	Kfs	Fl	Bt
V*	212.161	56.160	32.160	108.698	24.542	149.834
Al	5.48	0.14	0.00	1.00	0.00	2.65

*Molar volume (cm^3/mol) is calculated on the basis of composition in each mineral (see caption of Tables 1 and 3).

Table 5: Overall reactions leading to chloritization in the types A and B on the basis of the SVD analysis.

Type	【Conservation : constant volume (V) + closure components】 Overall reaction	Volume ratio of product minerals deduced from the overall reaction
Type A-1 **[CF1]***	**【V + Ti】** **0.810Bt + 0.453Al^{3+} + 0.718Fe^{2+} + 0.100Mn^{2+} + 0.248Mg^{2+} + 0.078Ca^{2+} + 3.933H_2O + 3.627H^+** → 0.508Chl + 0.083Ttn + 0.282Il + 1.567H_4SiO_4 + 1.554K^+ + 0.243F^- + 0.008Cl^-	Chl : Ttn : Il = 1 : 0.043 : 0.084
Type A-2 **[CF1]***	**【V + Al】** **0.592Bt + 0.100Fe^{2+} + 0.020 Mn^{2+} + 0.044Mg^{2+} + 0.757Ca^{2+} + 2.094H_2O + 4.722H^+ + 1.315F^-** → 0.333Chl + 0.734Fl + 1.448H_4SiO_4 + 0.213Ti^{2+} + 1.117K^+ + 0.006Cl^-	Chl : Fl = 1 : 0.255
Type A-3 **[CF1]***	**【V + Ti】** **0.806Bt + 0.411Al^{3+} + 0.550Fe^{2+} + 0.027Mn^{2+} + 0.057Mg^{2+} + 0.032Ca^{2+} + 2.934H_2O + 4.581H^+** → 0.530Chl + 0.264Il + 1.262H_4SiO_4 + 1.423K^+ + 0.129F^- + 0.024Cl^-	Chl : Il = 1 : 0.075
Type A-4 **[CF1]***	**【V + Ti + Mn】** **0.818Bt + 0.225Al^{3+} + 0.243Fe^{2+} + 0.214Mg^{2+} + 0.327Ca^{2+} + 2.698H_2O + 4.971H^+** → 0.487Chl + 0.293Ttn + 0.082Il + 0.017Fl + 1.355H_4SiO_4 + 1.547K^+ + 0.150F^- + 0.025Cl^-	Chl : Ttn : Il : Fl = 1 : 0.158 : 0.025 : 0.004
Type A-5 **[CF2]****	**【V + Ti + Mn】** **0.806Bt + 0.158Ca^{2+} + 0.005Na^+ + 0.216H_2O + 6.622H^+** → 0.269Chl + 0.161Ttn + 0.502Kfs + 1.401H_4SiO_4 + 0.485Al^{3+} + 0.739Fe^{2+} + 0.497Mg^{2+} + 1.069K^+ + 0.206F^- + 0.008Cl^-	Chl : Ttn : Kfs = 1 : 0.159 : 0.958
Type B-1 **[CF2]****	**【V + Ti + Mn】** **0.357Bt + 0.988Ca^{2+} + 0.943H_2O + 3.817H^+ + 1.714F^-** → 0.128Chl + 0.068Ttn + 0.923Fl + 1.222H_4SiO_4 + 0.329Al^{3+} + 0.346Fe^{2+} + 0.238Mg^{2+} + 0.704K^+ + 0.004Cl^-	Chl : Ttn : Fl = 1 : 0.139 : 0.836
Type B-2 **[CF1]***	**【V + Ti + Mn】** **0.765Bt + 0.362Al^{3+} + 0.050Mg^{2+} + 0.495Ca^{2+} + 3.082H_2O + 3.857H^+** → 0.417Chl + 0.495Ttn + 1.478H_4SiO_4 + 0.158Fe^{2+} + 1.469K^+ + 0.069F^- + 0.015Cl^-	Chl : Ttn = 1 : 0.313
Type B-3 **[CF2]****	**【V + Al】** **0.831Bt + 0.148Ti^{2+} + 0.002Mn^{2+} + 0.465Ca^{2+} + 0.004Na^+ + 2.044H_2O + 5.429H^+ + 0.016F^-** → 0.348Chl + 0.397Ttn + 0.083Il + 0.204Kfs + 0.064Fl + 1.679H_4SiO_4 + 0.530Fe^{2+} + 0.304Mg^{2+} + 1.362K^+ + 0.046Cl^-	Chl : Ttn : Il : Kfs : Fl = 1 : 0.302 : 0.036 : 0.300 : 0.021

*[CF1]: chlorite formation mechanism 1, **[CF2]: chlorite formation mechanism 2

Table 6: Two reaction parts (the chlorite formation and the formation of the associated minerals) constituting an overall reaction of the type A-1 with CF mechanism 1 and type A-5 with CF mechanism 2, respectively.

Type A-1 with 'CF mechanism 1'	
[Overall reaction] **0.810Bt + 0.453Al^{3+} + 0.718Fe^{2+} + 0.100Mn^{2+} + 0.248Mg^{2+} + 0.078Ca^{2+} + 3.933H_2O + 3.627H^+** → 0.508Chl + 0.083Ttn + 0.282Il + 1.567H_4SiO_4 + 1.554K^+ + 0.243F^- + 0.008Cl^-	
Chlorite formation (CF)	**0.810Bt + 0.434Al^{3+} + 0.514Fe^{2+} + 0.010Mn^{2+} + 0.247Mg^{2+} + 3.020H_2O + 5.723H^+** → 0.508Chl + 1.653H_4SiO_4 + 0.332Ti^{2+} + 1.555K^+ + 0.251F^- + 0.016Cl^-
Associated mineral formation (AMF)	**0.086H_4SiO_4 + 0.332Ti^{2+} + 0.019Al^{3+} + 0.204Fe^{2+} + 0.090Mn^{2+} + 0.022Mg^{2+} + 0.078Ca^{2+} + 0.001K^+ + 0.008F^- + 0.008Cl^- + 0.913H_2O** → 0.083Ttn + 0.282Il + 2.096H^+
Type A-5 with 'CF mechanism 2'	
[Overall reaction] **0.806Bt + 0.158Ca^{2+} + 0.005Na^+ + 0.216H_2O + 6.622H^+** → 0.269Chl + 0.161Ttn + 0.502Kfs + 1.401H_4SiO_4 + 0.485Al^{3+} + 0.739Fe^{2+} + 0.497Mg^{2+} + 1.069K^+ + 0.206F^- + 0.008Cl^-	
Chlorite formation (CF)	**0.806Bt + 2.118H_2O + 9.392H^+** → 0.269Chl + 3.082H_4SiO_4 + 0.129Ti^{2+} + 1.000Al^{3+} + 0.752Fe^{2+} + 0.497Mg^{2+} + 1.556K^+ + 0.218F^- + 0.008Cl^-
Associated mineral formation (AMF)	**1.681H_4SiO_4 + 0.129Ti^{2+} + 0.515Al^{3+} + 0.013Fe^{2+} + 0.158Ca^{2+} + 0.005Na^+ + 0.487K^+ + 0.011F^-** → 0.161Ttn + 0.502Kfs + 1.902H_2O + 2.770H^+

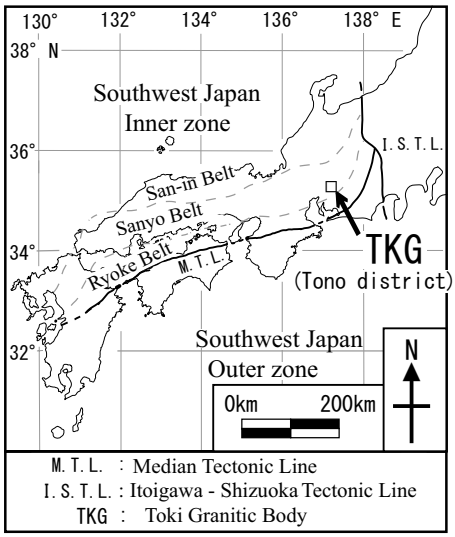

Yuguchi et al. Fig. 1

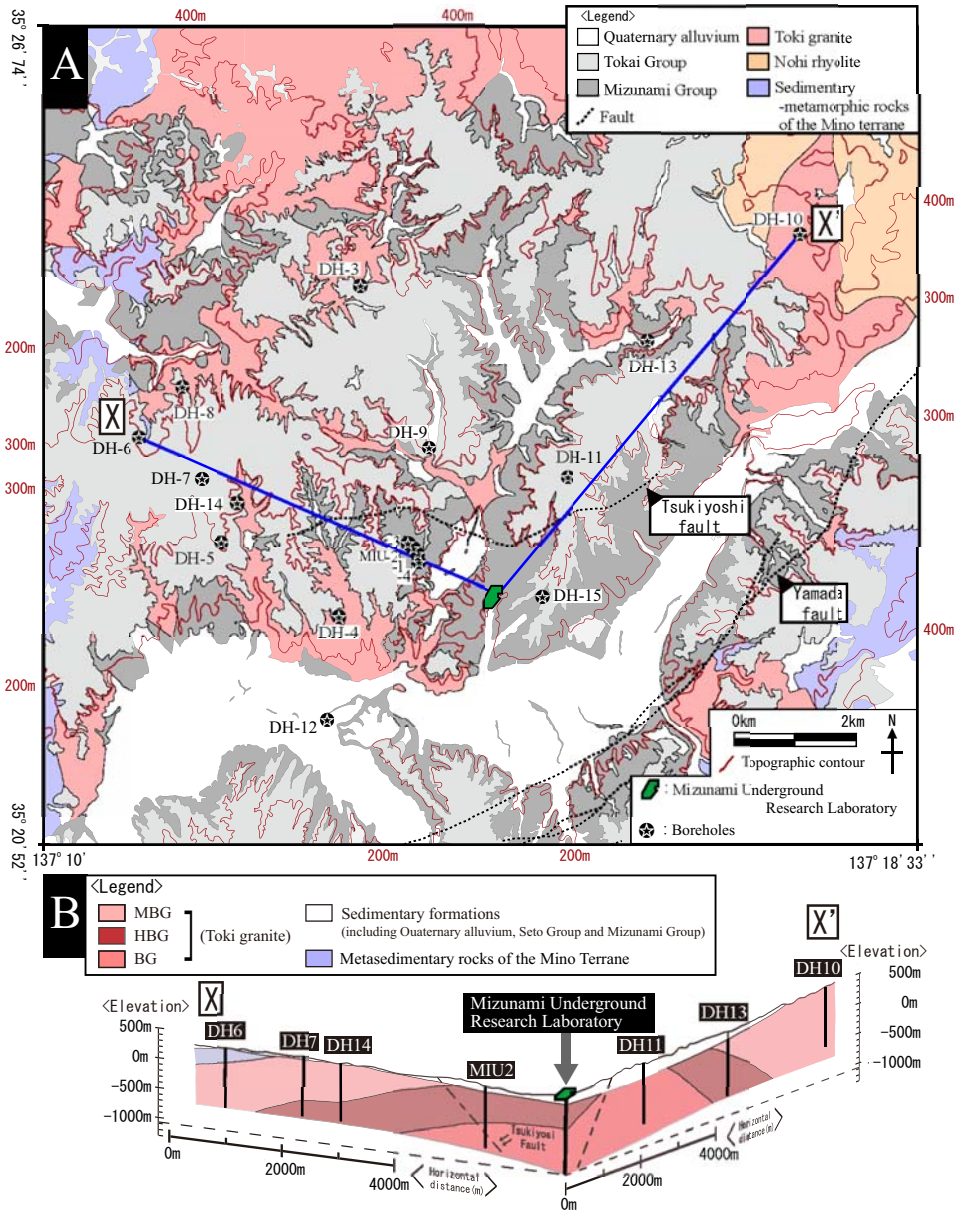

Yuguchi et al. Fig. 2

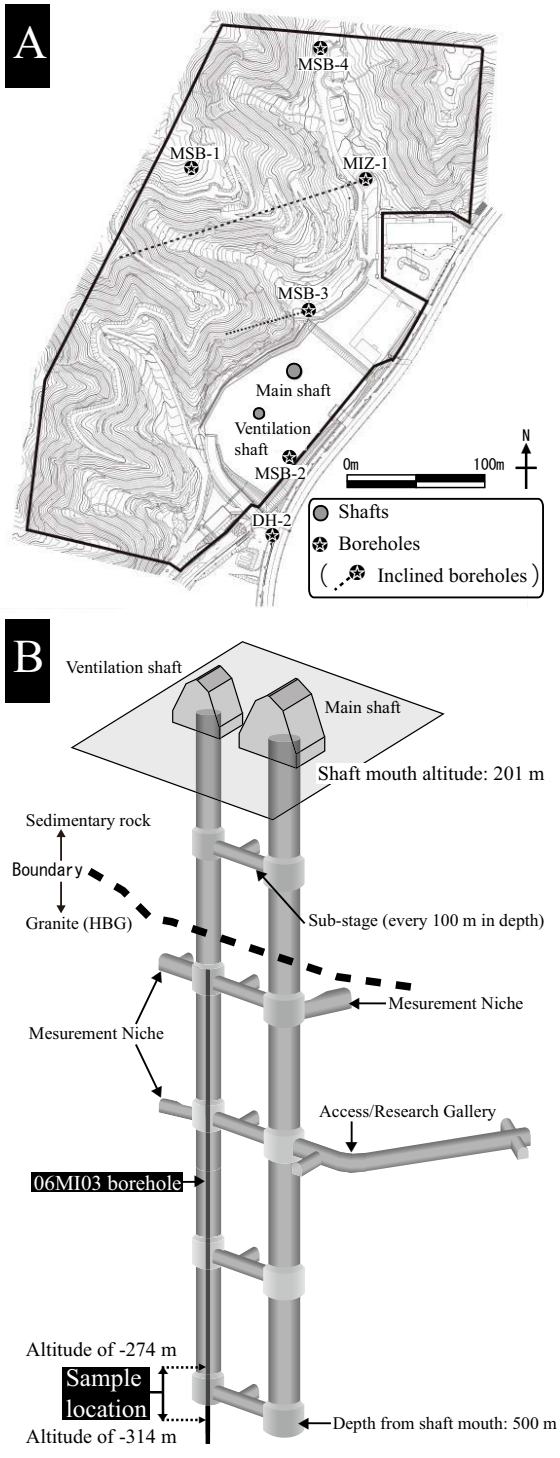

Yuguchi et al. Fig. 3

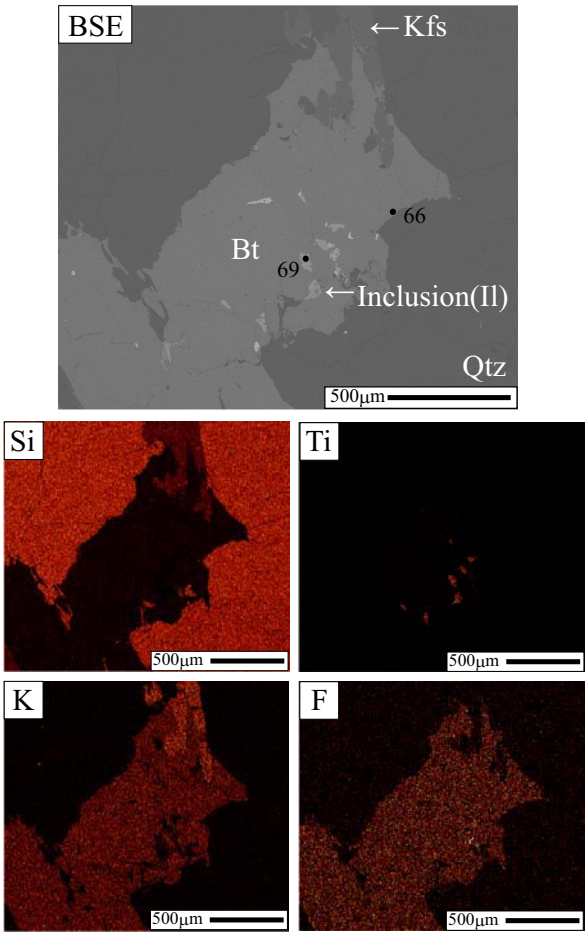

Yuguchi et al. Fig. 4

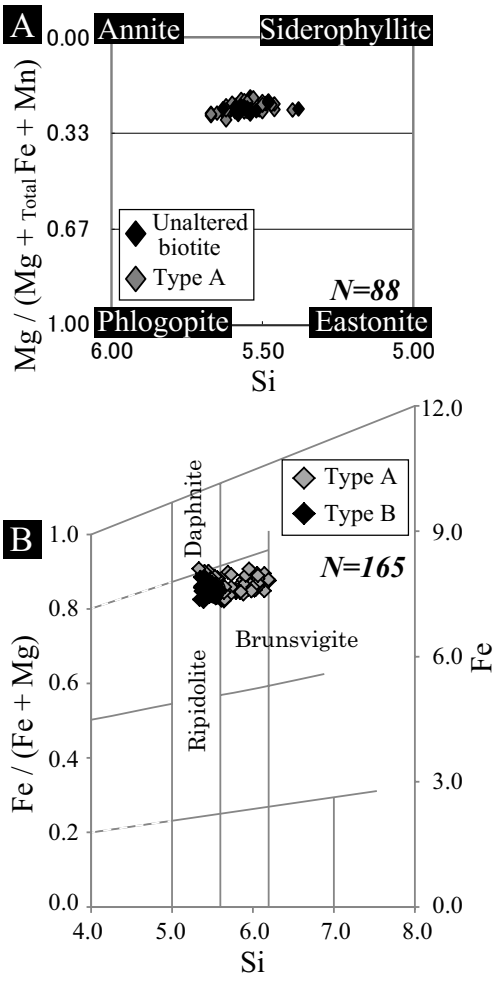

Yuguchi et al. Fig. 5

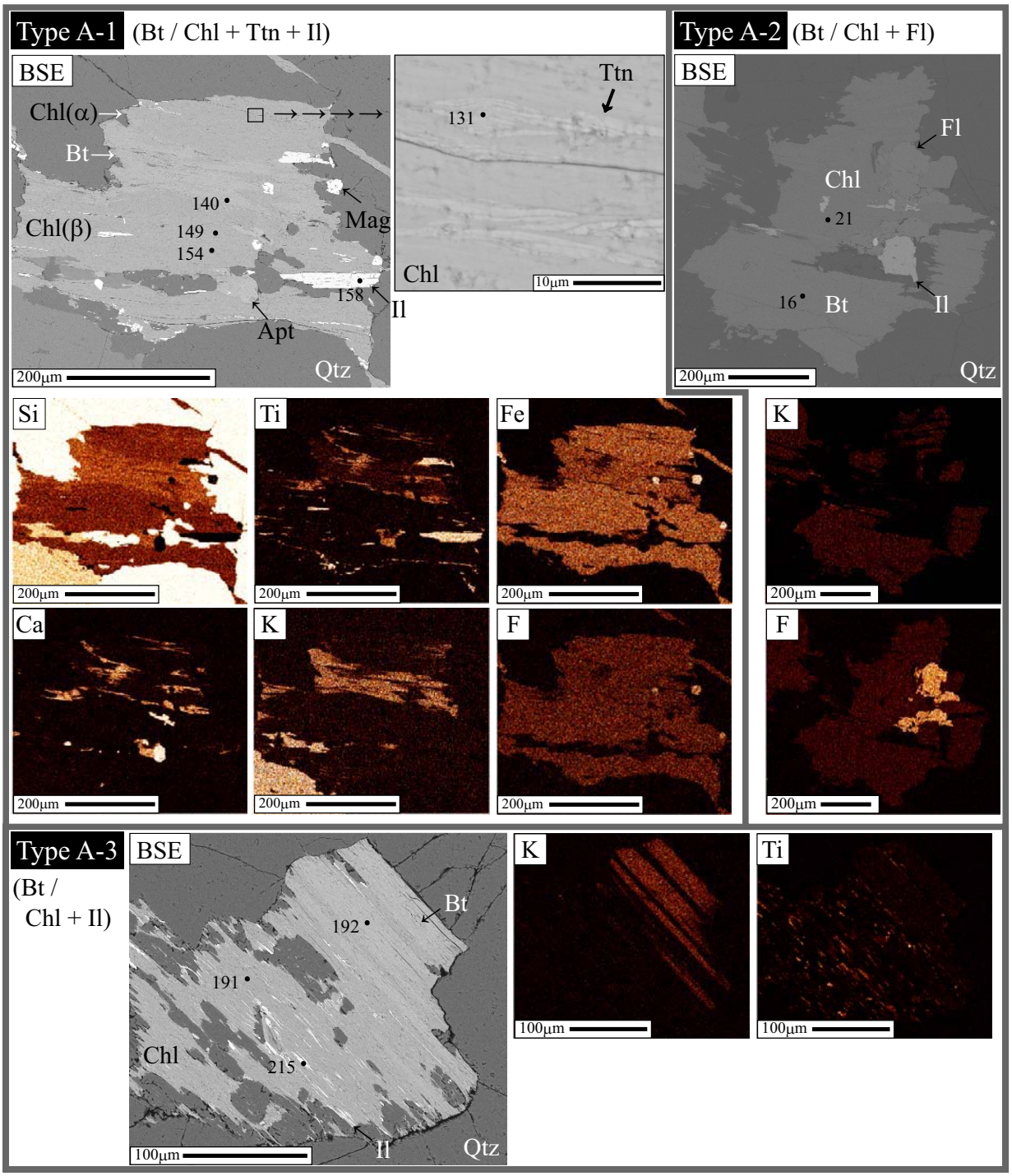

Yuguchi et al. Fig. 6

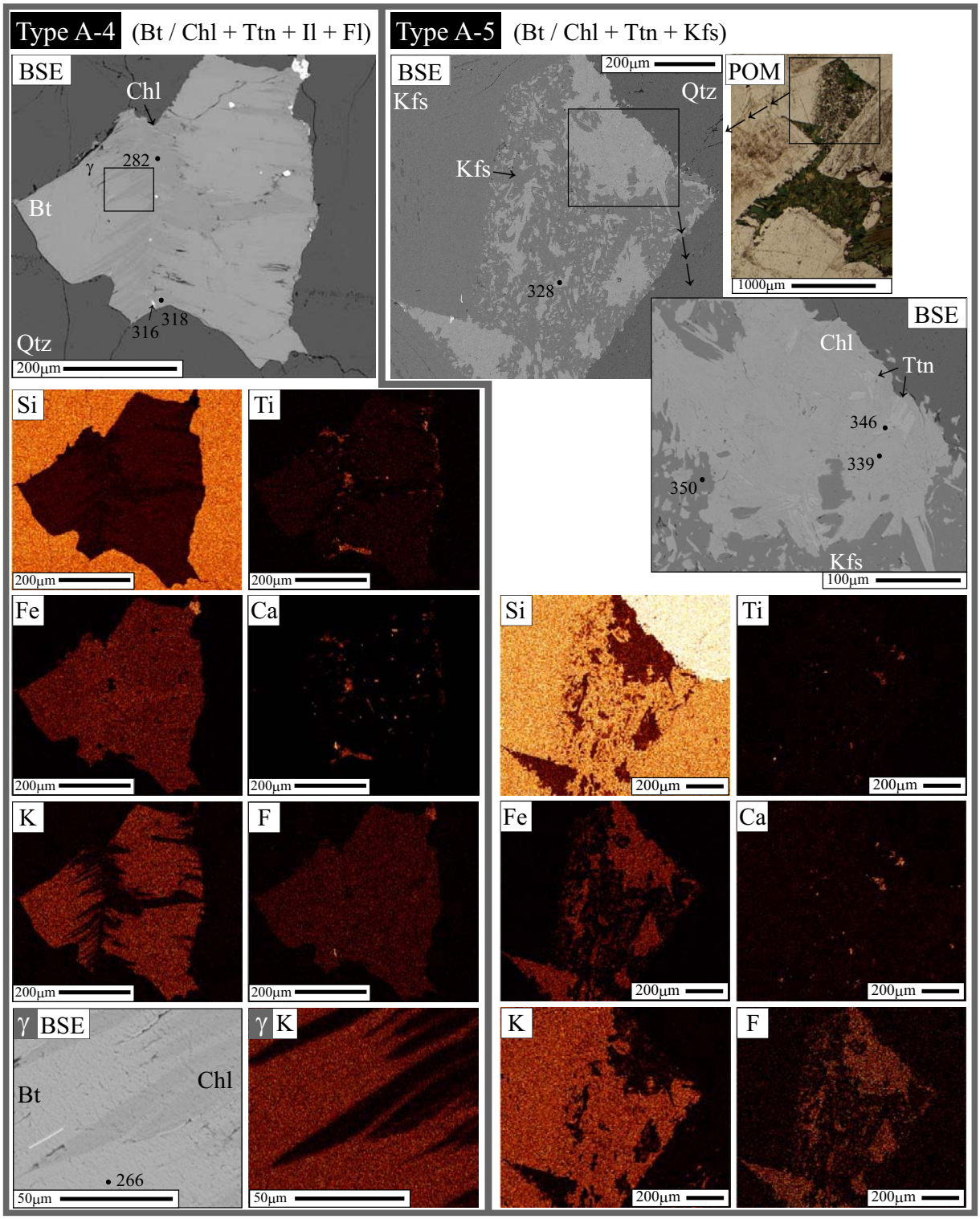

Yuguchi et al. Fig. 6 continued

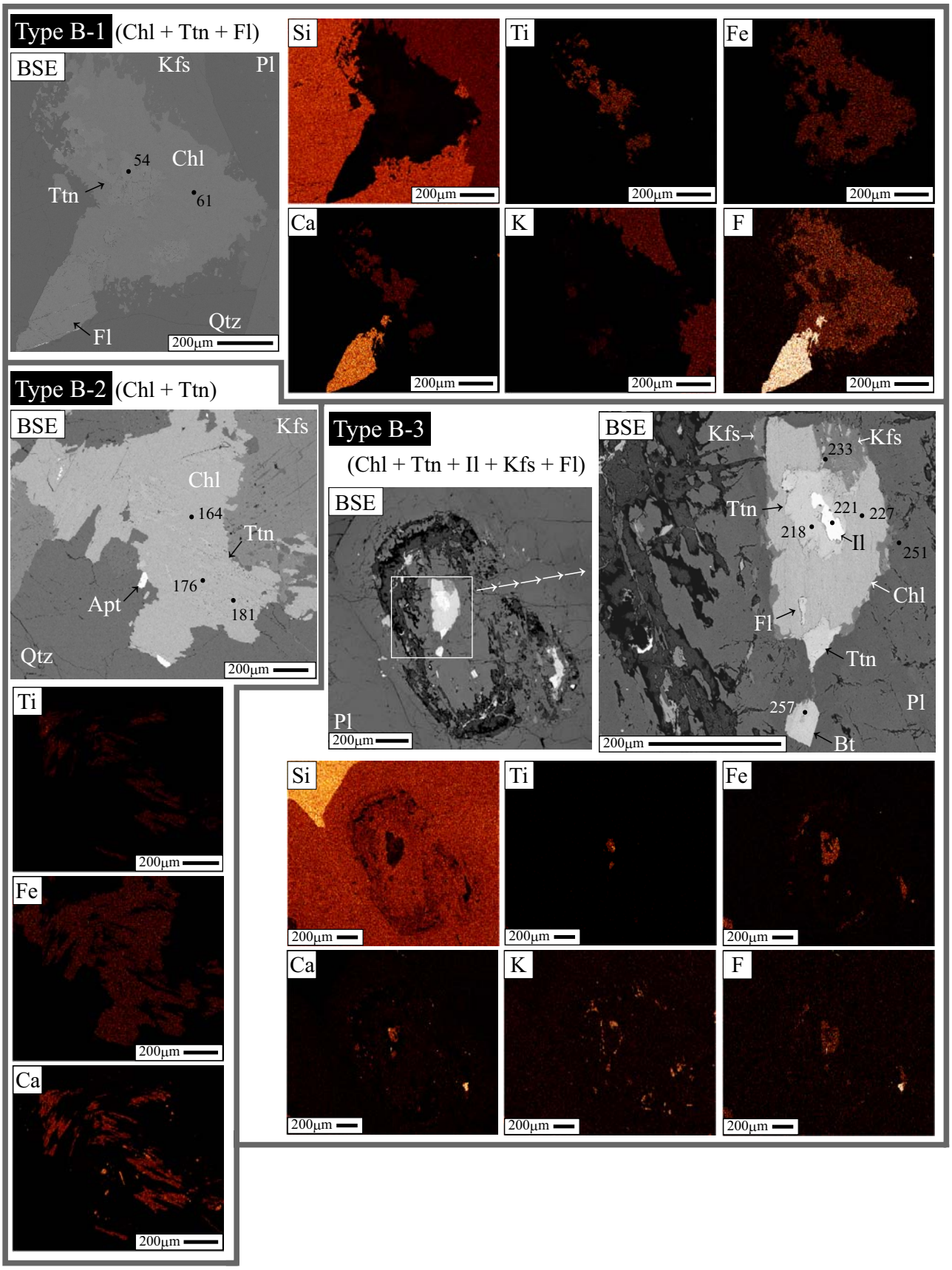

Yuguchi et al. Fig. 7

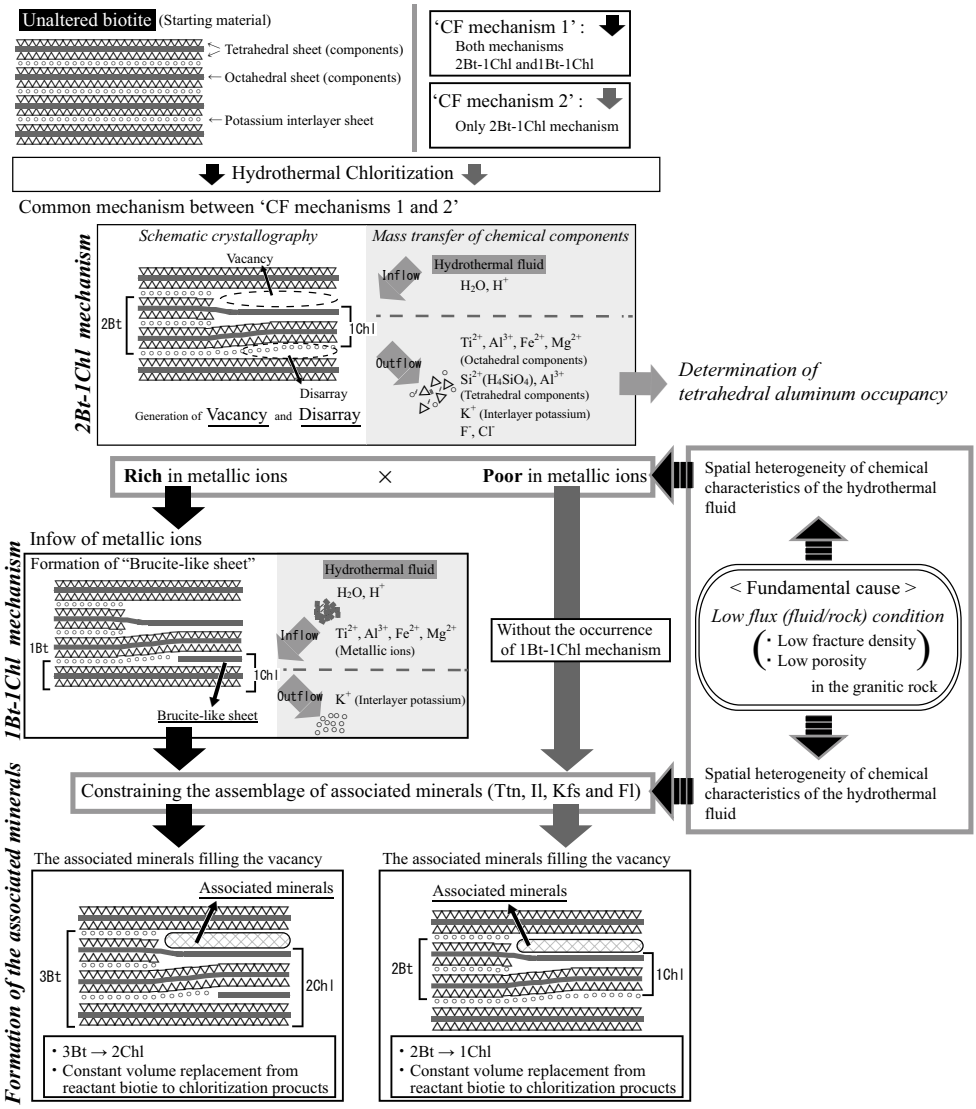

Yuguchi et al. Fig. 8

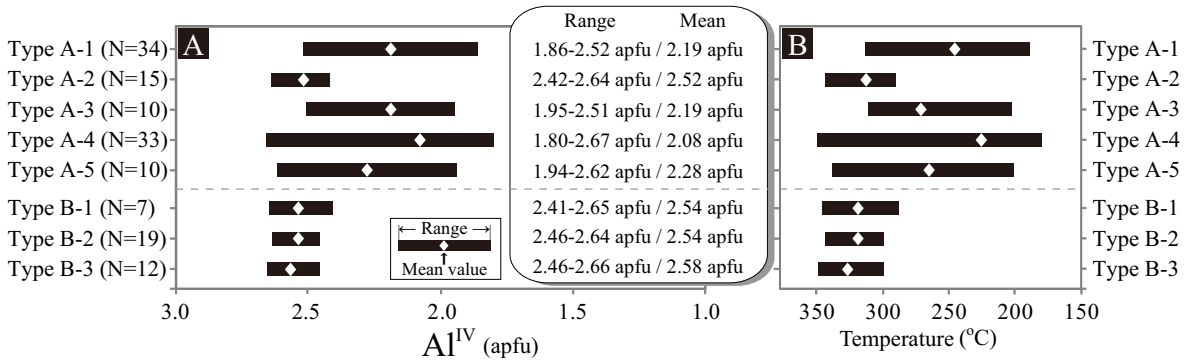

Yuguchi et al. Fig. 9

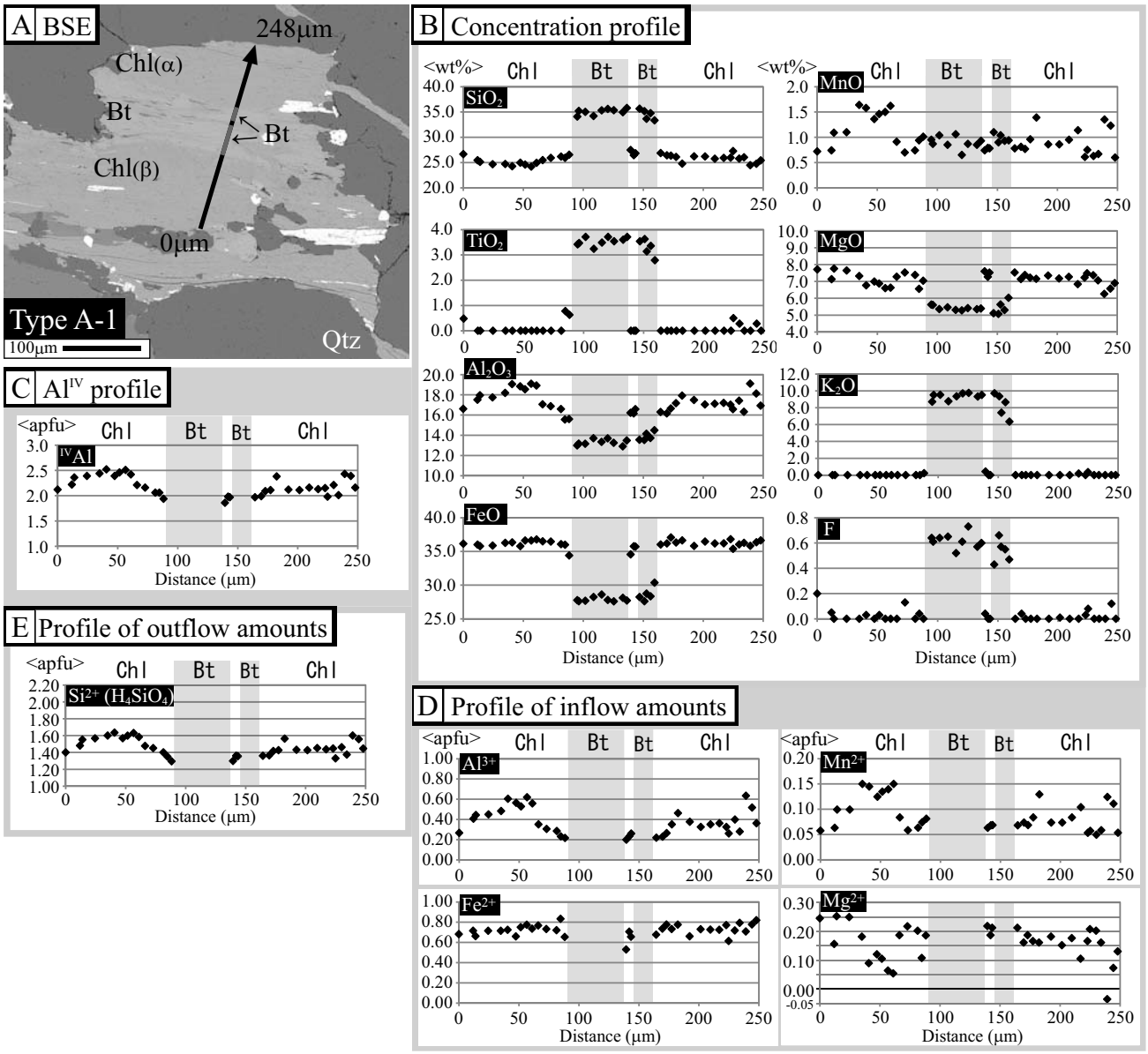

Yuguchi et al. Fig. 10